

**ISTANBUL TECHNICAL UNIVERSITY ★ GRADUATE SCHOOL OF SCIENCE**  
**ENGINEERING AND TECHNOLOGY**

**INVESTIGATION OF NANOSTRUCTURED VANADIUM OXIDES BY WET  
CHEMICAL PROCESSING: STRUCTURAL, MORPHOLOGICAL, OPTICAL,  
AND ELECTROCHEMICAL ANALYSIS**



**M.Sc. THESIS**

**Musa EROL**

**Department of Nanoscience and Nanoengineering**

**Nanoscience and Nanoengineering Programme**

**JUNE 2017**



**ISTANBUL TECHNICAL UNIVERSITY ★ GRADUATE SCHOOL OF SCIENCE**  
**ENGINEERING AND TECHNOLOGY**

**INVESTIGATION OF NANOSTRUCTURED VANADIUM OXIDES BY WET  
CHEMICAL PROCESSING: STRUCTURAL, MORPHOLOGICAL, OPTICAL,  
AND ELECTROCHEMICAL ANALYSIS**

**M.Sc. THESIS**

**Musa EROL  
(513131029)**

**Department of Nanoscience and Nanoengineering**

**Nanoscience and Nanoengineering Programme**

**Thesis Advisor: Professor Esra ÖZKAN ZAYİM**

**JUNE 2017**



**İSTANBUL TEKNİK ÜNİVERSİTESİ ★ FEN BİLİMLERİ ENSTİTÜSÜ**

**SIVI-HAL YÖNTEMİ İLE ELDE EDİLEN NANOYAPILI VANADYUM  
OKSİTLERİN İNCELENMESİ: YAPISAL, MORFOLOJİK, OPTİK VE  
ELEKTROKİMYASAL ANALİZ**

**YÜKSEK LİSANS TEZİ**

**Musa EROL  
(513131029)**

**Nanobilim ve Nanomühendislik Anabilim Dalı**

**Nanobilim ve Nanomühendislik Programı**

**Tez Danışmanı: Prof. Dr. Esra ÖZKAN ZAYİM**

**HAZİRAN 2017**



Musa EROL, a M.Sc. student of ITU Graduate School of Science Engineering and Technology student ID 513131029, successfully defended the thesis/dissertation entitled “INVESTIGATION OF NANOSTRUCTURED VANADIUM OXIDES BY WET CHEMICAL PROCESSING: STRUCTURAL, MORPHOLOGICAL, OPTICAL, AND ELECTROCHEMICAL ANALYSIS”, which he prepared after fulfilling the requirements specified in the associated legislations, before the jury whose signatures are below.

**Thesis Advisor :**     **Professor Esra ÖZKAN ZAYİM**     .....  
Istanbul Technical University

**Jury Members :**     **Professor Nilgün YAVUZ**     .....  
Istanbul Technical University

**Asst. Prof. Saffettin YILDIRIM**     .....  
Istanbul University

**Date of Submission : 5 May 2017**  
**Date of Defense : 8 June 2017**





*to Esmâ, Hayrunnisa, and Aişe,*



## **FOREWORD**

I wish to express my deep gratitude to my advisor, Professor Esra Ö.ZAYİM, for her guidance in my PhD journey that consists of challenges and interests. I appreciate her not only the broad knowledge and sharp scientific instinct, but also optimistic and confident personality, which helped me very much to finish my work.

I would like to thank Prof. Esmâ SEZER, Prof. Nilgün K.YAVUZ, Asst. Prof. Dr. Filiz ALTAY and her assistant Nagihan OKUTAN for their collaboration in several topics and also thank all other people who directly and indirectly contributed to my thesis.

Especially, I would like to thank my friends in the ITU, Ömer EROĞLU and Duygu KALKAN for their collaboration and friendship.

May 2017

Musa EROL  
(Material Science and Engineer)



## TABLE OF CONTENTS

	<u>Page</u>
<b>FOREWORD</b> .....	<b>ix</b>
<b>TABLE OF CONTENTS</b> .....	<b>xi</b>
<b>ABBREVIATIONS</b> .....	<b>xiii</b>
<b>SYMBOLS</b> .....	<b>xv</b>
<b>LIST OF TABLES</b> .....	<b>xvii</b>
<b>LIST OF FIGURES</b> .....	<b>xix</b>
<b>SUMMARY</b> .....	<b>xxi</b>
<b>ÖZET</b> .....	<b>xxiii</b>
<b>1. INTRODUCTION</b> .....	<b>1</b>
<b>2. THEORETICAL PART</b> .....	<b>5</b>
2.1 Vanadium .....	5
2.2 Vanadium-Oxygen System .....	6
2.2.1 Vanadium(VI) oxide, VO <sub>2</sub> .....	11
2.3 Thin Film Production Methods .....	12
2.3.1 Chemical vapor deposition.....	13
2.3.2 Physical vapor deposition .....	13
2.3.3 Wet-coating (sol-gel) .....	15
2.3.3.1 Electrodeposition.....	17
2.3.3.2 Dip-coating.....	17
2.3.3.3 Spin-coating .....	18
2.3.4 Electrospinning .....	19
2.3.4.1 Electrospinning parameters .....	20
<b>3. EXPERIMENTAL PART</b> .....	<b>25</b>
3.1 Reagents and Substrate Preparation .....	25
3.2 Solution Preparation .....	26
3.2.1 Solution Characterization.....	27
3.3 Nanofiber and Thin Film Deposition .....	31
3.4 Electrochemical Characterization.....	32
3.5 Structural and Morphological Characterization .....	32
<b>4. RESULT AND DISCUSSION</b> .....	<b>35</b>
4.1 Structural and Morphological Analysis.....	35
4.1.1 X-ray powder diffraction characterization .....	35
4.1.2 Transmission electron microscopy investigations .....	36
4.1.3 Surface morphology by scanning electron microscopy .....	39
4.2 Optical Properties .....	43
4.3 Electrochemical Properties.....	45
4.3.1 Cyclic voltammetry .....	45
4.3.2 Electrochemical impedance spectroscopy analysis.....	50
<b>5. CONCLUSION</b> .....	<b>57</b>
<b>REFERENCES</b> .....	<b>61</b>
<b>CURRICULUM VITAE</b> .....	<b>65</b>



## ABBREVIATIONS

<b>PVP</b>	: Poly-(vinylpyrrolidone)
<b>STM</b>	: Semiconductor to metal transition
<b>SEM</b>	: Scanning electron microscopy
<b>TEM</b>	: Transmission electron microscopy
<b>EIS</b>	: Electrochemical impedance spectroscopy
<b>CV</b>	: Cyclic voltammetry/voltammogram
<b>V-O</b>	: Vanadium-oxygen
<b>CVD</b>	: Chemical vapor deposition
<b>PVD</b>	: Physical vapor deposition
<b>PECVD</b>	: Plasma enhancing chemical vapor deposition
<b>ITO</b>	: Indium doped tin oxide glass
<b>ITO-PET</b>	: Indium tin oxide coated polyethylene terephthalate film
<b>UV-Vis</b>	: UV-visible spectrophotometer/spectroscopy
<b>XRD</b>	: X-ray powder diffraction



## SYMBOLS

<b>t</b>	: Film thickness
<b>c</b>	: Rate constant
<b><math>\eta</math></b>	: Viscosity
<b><math>v</math></b>	: Velocity
<b>g</b>	: Gravity acceleration
<b><math>\rho</math></b>	: Density
<b><math>\tau</math></b>	: Shear stress
<b>K</b>	: Consistency index
<b><math>\dot{\gamma}, \dot{\gamma}_{max}</math></b>	: Shear rate, maximum shear rate
<b>n</b>	: Flow behavior index
<b>Q</b>	: Volumetric flow rate
<b>R</b>	: Inside radius of a tube



## LIST OF TABLES

	<u>Page</u>
<b>Table 2.1</b> : Some properties of single-valance vanadium oxides.....	7
<b>Table 3.1</b> : The measured properties of the solutions. ....	30
<b>Table 3.2</b> : List of the deposited samples. ....	31
<b>Table 4.1</b> : Peak potential and current density, intercalation/deintercalation capacity as deduced from the CV at a scan rate of 10 mV/s, together with differences in current densities of cathode and corresponding anode peaks. ....	49
<b>Table 4.2</b> : Fitting values of the modelled equivalent circuit elements by the simulation of the Nyquist plots of annealed samples. ....	55



## LIST OF FIGURES

	<u>Page</u>
<b>Figure 2.1</b> : Free vanadium metal (left), vanadinite (middle), and a presentation of crystal structure of vanadium, BCC (right). .....	5
<b>Figure 2.2</b> : Aqueous solution of +2, +3, +4 and +5 ions of vanadium. ....	6
<b>Figure 2.3</b> : Vanadium-oxygen phase diagram; the whole range (top), and low oxygen content (bottom).....	8
<b>Figure 2.4</b> : The change in conductivity versus reciprocal temperature for some materials exhibiting SMT. ....	9
<b>Figure 2.5</b> : Sketch of an EC device, showing typical materials and the movement of ions.....	10
<b>Figure 2.6</b> : Switchable motorcycle helmet visor made. The spectra (right) shows the change in visible properties with an applied voltage of 1.6 V.....	10
<b>Figure 2.7</b> : Comparison of the crystal structures of VO <sub>2</sub> (M1) (left) and VO <sub>2</sub> (R) (right). Red balls represents vanadium atoms, while blue balls are oxygen atoms.....	11
<b>Figure 2.8</b> : Schematic phase diagram of VO <sub>2</sub> . ....	12
<b>Figure 2.9</b> : Schematic illustration of the preparation of various kinds of materials by sol-gel method. ....	16
<b>Figure 3.1</b> : A schematic representation of the preparation of solutions. ....	27
<b>Figure 3.2</b> : UV-visible spectra of the Sol-A at different times.....	28
<b>Figure 3.3</b> : Viscosity values versus shear rates of the prepared solutions. Right y-axis gives the viscosity value of Sol-B and Sol-C. ....	30
<b>Figure 4.1</b> : XRD patterns of the SC-A0, SC-A500, SC-B0, SC-B500, SC-C0 and SC-C500 from bottom to top, respectively. ....	35
<b>Figure 4.2</b> : The BF-TEM images and SAED patterns of the SC samples. ....	37
<b>Figure 4.3</b> : BF-TEM images at higher magnification from the nano crystals weakly presented in the SC-A and from the precipitations observed in the SC-C500 (lighter quadrilateral in the sheet grain). ....	38
<b>Figure 4.4</b> : The average intensity over circles in the function the scattering vector based on the polycrystalline SAED patterns of the SC-A, SC-B, SC-C and SC-C500 samples. The perpendicular lines indicate the locations of the V <sub>6</sub> O <sub>13</sub> structure and the [001] textured VO <sub>2</sub> structure, based on XRD data. ....	39
<b>Figure 4.5</b> : SEM micrographs of NF-A0. ....	40
<b>Figure 4.6</b> : SEM micrographs of electrospayed films that annealed at 500°C.....	40
<b>Figure 4.7</b> : SEM images of SC-A500. ....	41
<b>Figure 4.8</b> : 5K (left) and 20K (right) magnified SEM micrographs of SC-B0 (top) and SC-C0 (bottom).....	42
<b>Figure 4.9</b> : 5K (left) and 20K (right) magnified SEM images of SC-B500 (top) and SC-C500 (bottom). ....	42
<b>Figure 4.10</b> : Transmittance spectra of all samples coated on microscope slides within the range of 300 - 900 nm of wavelength. ....	44
<b>Figure 4.11</b> : Temperature dependent transmittance spectra of SC-B500.....	44

<b>Figure 4.12</b> : Temperature dependent transmittance spectra of SC-C500 .....	<b>45</b>
<b>Figure 4.13</b> : Cyclic voltammogram of NF-A500.....	<b>47</b>
<b>Figure 4.14</b> : Cyclic voltammogram of SC-A500.....	<b>47</b>
<b>Figure 4.15</b> : Cyclic voltammogram of SC-B500 .....	<b>48</b>
<b>Figure 4.16</b> : Cyclic voltammogram of SC-C500 .....	<b>48</b>
<b>Figure 4.17</b> : Cyclic voltammogram of annealed samples at a scan rate of 10 mV/s. .....	<b>50</b>
<b>Figure 4.18</b> : Nyquist plots of the annealed samples. Left top: NF-A500, right top: SC-A500, left bottom: SC-B500, right bottom: SC-C500.....	<b>51</b>
<b>Figure 4.19</b> : Bode Phase plots of annealed samples. ....	<b>51</b>
<b>Figure 4.20</b> : Schematic representation of electrochemical experimental setup, and equivalent circuit modelling of vanadium-oxide/SnO <sub>2</sub> :In electrodes (inside). ....	<b>53</b>
<b>Figure 5.1</b> : Electrochromic photograph of SC-B500 film taken at 700, 300, and -200 mV applied potentials from left to right, respectively. ....	<b>58</b>



# **INVESTIGATION OF NANOSTRUCTURED VANADIUM OXIDES BY WET CHEMICAL PROCESSING: STRUCTURAL, MORPHOLOGICAL, OPTICAL, AND ELECTROCHEMICAL ANALYSIS**

## **SUMMARY**

Material science steers the technological advancements. Even prehistoric ages are called as materials' names. Nano- and thin film materials took place of the normal/bulk materials, nowadays. Thus, in order to product nano-sized/ nano-structured materials and manipulate materials at nano scale, a new discipline is developed, which is called nanotechnology.

There are many methods to produce thin films, such as chemical vapor deposition, physical vapor deposition, atomic layer deposition, spray pyrolysis, sol-gel method, etc. Among these methods, sol-gel is one of the most used method because it is economical and easy way. A wet solution, called gel, is obtained with sol-gel method, which is then deposited onto a substrate by some techniques, such as dip-coating, electrodeposition, spin-coating etc. Spin-coating technique is superior among other techniques because it leads to atomic packing in one direction.

Nanofibers, which are 1D materials, are one of the most interesting materials among nanostructures due to their versatility, high surface area, high aspect ratio, high porosity, high electrical conductivity in one direction, etc. Electrospinning is most used method to produce nanofibers from lab-scale to industrial scale. However, there are many parameters effecting the characteristics of the obtained fibers in electrospinning technique.

Vanadium and its oxide form has been studied for a long time due to their interesting characteristics. The reason of such great interest drawn to vanadium and its oxide forms is based on the varied oxidation states from +2 to +5 which let it form many oxide forms, and also the variability of the oxygen coordination geometries, such as octahedral, square pyramids, tetrahedral etc. These characteristics let vanadium oxides yield an impressive variety of structural and crystallographic arrangements. VO<sub>2</sub> exhibits a semiconductor to metal transition near to room temperature, at about 70°C. V<sub>2</sub>O<sub>5</sub> has an orthorhombic crystalline structure with a layered structure, which promises high ratio ion intercalation. Thus, it is very interesting material for electrochemical applications such as li-ion batteries, supercapacitors, sensors, etc.

In this study, we prepared eight different vanadium-oxide samples (6 samples in thin-film form, and the other 2 samples in nanofiber form) from three different solutions/gels. We characterized the samples by x-ray powder diffractometer (XRD), scanning electron microscopy (SEM), transmission electron microscopy (TEM), UV-visible spectrophotometer (UV-Vis), cyclic voltammetry (CV), electrochemical impedance spectroscopy (EIS). Additionally, thermochromic properties of annealed samples were investigated. We also characterized solutions by analyzing their conductivity, surface tension, viscosity and optical properties.



# SIVI-HAL YÖNTEMİ İLE ELDE EDİLEN NANOYAPILI VANADYUM OXİTLERİN İNCELENMESİ: YAPISAL, MORFOLOJİK, OPTİK VE ELEKTROKİMYASAL ANALİZ

## ÖZET

Malzeme bilimi teknolojik ilerlemeye ve hatta insanlığın gelişimine yön vermektedir. Bu sebeple tarih öncesi çağlar malzeme isimleri ile isimlendirilmişlerdir. Günümüzde, nano- ve ince film malzemeleri normal makro boyutlu malzemelerin yerini almıştır. Bu yüzden nano-yapılı (veya nano-boyutta) ve ince film malzemeler üretmek ve malzemeleri nanoboyutta işleyebilmek için nanoteknoloji olarak adlandırılan yeni bir disiplin geliştirilmiştir.

Kimyasal buhar biriktirme, fiziksel buhar biriktirme, sol-jel v.b gibi pek çok ince film üretim metodu bulunmaktadır. Bunların arasında sol-jel tekniği en çok kullanılan yöntemlerden bir tanesidir. Sol-jel metodunun yaygın olmasının temel sebepleri ekonomik ve kolay olmasıdır. Sol-jel metodu ile jel olarak da adlandırılan sıvı bir çözelti elde edilir ve bu çözelti daldırarak kaplama, elektrodepozisyon, dödürerek kaplama v.b gibi tekniklerle bir altaş malzeme üzerine ince film formunda kaplanır. Dödürerek kaplama tekniği, atomların belirli bir yönde dizilimine olanak tanimasından dolayı diğerlerine oranla daha çok tercih edilen bir yöntemdir.

1B yapıda olan nanofiberler; çok yönlülük, yüksek yüzey alanı, yüksek gözeneklilik, yüksek en boy oranı, tek yönde daha yüksek elektriksel iletkenlik vb. Gibi özelliklerinden dolayı nano-yapılar arasında en çok ilgi çeken yapılardan bir tanesidir. Elektrodöndürme yöntemi laboratuvar ölçeğinden endüstriyel üretime kadar en çok kullanılan nanofiber üretim tekniklerinden bir tanesidir. Ancak, elektrodöndürme yönteminde nihai fiberin özelliklerini etkileyen çok fazla parametre vardır.

Vanadyum ve oksit yapıları ilgi çekici özelliklerinden dolayı çok uzun zamandır araştıma konusudur. Vanadyum ve oksitli yapılarını ilginç kılan temel sebepler şunlardır; vanadyumun +2'den +5'e kadar pek çok değerliğe sahip olması, ki bu özellik vanadyumun pek çok oksit formu oluşturmasını sağlamaktadır, diğer özelliği ise vanadyumun oktahedra, tetrahedral, kare piramit vb. gibi pek çok oksijen koordinasyon geometrisine sahip olmasıdır. Bu özellikler, vanadyum oksitlerin, etkileyici çeşitli yapısal ve kristalografik yapılarda olmalarını sağlamaktadır. VO<sub>2</sub>, oda sıcaklığına yakın bir sıcaklıkta, yaklaşık 70°C'de, yarı iletken – metal dönüşümü karakteristiğine sahiptir. VO<sub>2</sub>, 70°C'nin altında yarı-iletken özellikleri göstermekte iken, 70°C üzerinde metal gibi davranmaktadır. VO<sub>2</sub>'nin elektriksel, optik vb. gibi bazı fiziksel özellikleri 70°C'de büyük bir değişim göstermektedir. V<sub>2</sub>O<sub>5</sub>, katmanlı yapıdadır ve ortorombik kristal yapıya sahiptir. Katmanlı yapısı sayesinde daha çok iyonun yapıya girişine izin vermektedir. Bu sebeple, V<sub>2</sub>O<sub>5</sub>, li-ion bataryalar, sensörler, süper-kapasitörler vb. gibi elektrokimyasal uygulamalar için çok ilgi çekici bir malzemedir. V<sub>6</sub>O<sub>13</sub> ise, V<sub>2</sub>O<sub>5</sub>'inkine benzer ancak daha düzenli bir kristal yapıya sahiptir, ve aynı V<sub>2</sub>O<sub>5</sub> gibi katmanlı yapıya sahiptir.

Bu çalışmada, 3 farklı çözüldüden/jelden 6'sı ince film yapıda, diğeri 2'si nanofiber yapıda olmak üzere toplam 8 vanadyum-oksit numunesi başarı ile üretilmiştir. Bu numuneler; x-ray toz difraksiyonu (XRD), taramalı elektron mikroskopu (SEM), geçirimli elektron mikroskopu (TEM), UV-görünür bölge spektrofotometresi (UV-Vis), dönüşümlü voltametri (CV) ve elektrokimyasal impedans spektroskopisi (EIS) yöntemleri ile analiz edilmiştir. Ayrıca, ısıtma işlemi uygulanmış numunelerin termokromik özellikleri incelenmiştir. Çözüldülerin iletkenlik, yüzey gerilimi, viskozite ve optik özellikleri araştırılarak karakterize edilmişlerdir.

İlk çözüldü şu şekilde hazırlanmıştır: önce 0.1 gr  $V_2O_5$  tozu 4 ml %3'lük seyreltilmiş  $H_2O_2$  çözüldüsünde çözüldürülmüş, daha sonra bu çözüldüye poly –(vinilpirolidon) (PVP) eklenerek tüm içerik çözüldüne kadar karıştırılmıştır. Bu çözüldü kullanılarak elektroçizme yöntemi ile nanofiber elde edilmiştir. SEM resimlerine göre yoğun bir nanofiber yapısı gözlenmektedir. Elde edilen nanofiberler; pürüzsüz ve düzgün yüzeye, yüksek en-boy oranına, ve tüm alan boyunca düzenli çapa sahiptir. Elde edilen numunede ayrıca yoğun boncuk yapısı ve görece büyük bazı damlacıklar gözlenmektedir. Boncuklu yapının oluşumu çözüldünün düşük viskoziteye sahip olmasından, ve uygulanan voltajın yüksekliğinden kaynaklandığı düşünülmüştür. Boncuklu yapının oluşuma ihtimalinin fiber çapı küçüldükçe arttığı iyi bilinmektedir. Elde edilen nanofiberlerin çapları 15 – 240 nm arasında değişmektedir –ki bu değerler çok ince sayılır–, bunun sonucunda boncuklu yapı doğal olarak oluşmuştur. Boncuklu yapıdan kurtulmak için yapılan deneylerde, nem oranının çok daha yüksek olmasından dolayı nanofiber elde edilememiştir. Ancak, çözüldünün yüksek nem oranına sahip havada hidrolize olmasından dolayı çayır-yapıda (grassland) nanorodlar elde edilmiştir. Nanorodların genişlikleri 250 – 640 nm arasında değişirken, uzunlukları 1 – 5  $\mu m$  arasındadır.

İlk çözüldü ile ayrıca ince film de üretilmiştir. Çözüldü, döndürerek kaplama tekniği ile 1500 rpm'de 2 dk döndürülerek, corning cam veya ITO üzerinde film olarak biriktirilmiştir. Film 500°C'de hava atmosferinde 1 saat boyunca kalsine edilmiştir. SEM resimlerine göre; ısıtma işlemi uygulanmamış film son derece pürüzsüz ve düzgün bir yüzeye sahipken, kalsinasyon işlemine uygulanınca numune üniform dağılmış gözeneklerle birlikte damar (yapraklarda bulunan) benzeri bir morfolojiye dönüşmüştür. Damar yapısı, PVP'nin yapıdan uzaklaşmasıyla oluşan gözeneklerin bölmediği bir sürekli faz gibi gözlenmektedir. Ayrıca, herhangi bir aglomerasyon, parçacık oluşumu veya çatlak gözlenmemektedir. XRD sonuçlarına göre ısıtma işlemi uygulanmamış film amorf yapıya sahipken, kalsinasyon işlemi ile birlikte yapıda az da olsa kristallenme olmuştur, yapıdaki PVP'nin varlığı kristallenmeyi engellemiştir.

İkinci başlangıç sıvısı şu şekilde hazırlanmıştır; önce 0.1 gr  $V_2O_5$  tozu 4 ml %3'lük seyreltilmiş  $H_2O_2$  çözüldüsünde çözüldürülmüş, daha sonra bu çözüldüye 80°C'de 1 saat boyunca ısıtma işlemi uygulanmıştır. Isıtma işlemi birlikte, çözüldü hava ile hidrolize olarak polikondansasyon reaksiyonuna uğrayıp jelleşmiştir. Elde edilen jel döndürerek kaplama tekniği ile 3000 rpm'de 3 dk boyunca döndürülerek alttaş üzerine film olarak kaplanmıştır ve film 500°C'de hava atmosferinde ısıtma işlemi maruz bırakılmıştır. SEM resimlerine göre ısıtma işlemi öncesinde “spindle” benzeri film yüzeyi oluşmuştur. Bu yüzeyin boğçalanmış “rod”lardan kaynaklandığı düşünülmektedir. Tavlamadan sonra ise film, düzlemsel büyümüş nanorodlu bir yapıya dönüşmüştür. Bu nanorodların genişlik ve uzunlukları sırası ile 250 – 500 nm ve 1 – 3.1  $\mu m$  olarak ölçülmüştür. XRD analizine göre ısıtma işlemi uygulanmamış film amorf yapıda iken tavlama işlemi yüksek kristaliniteye sahiptir.

Üçüncü başlangıç sıvısı ise ikinci jelin 10 gün boyunca oda sıcaklığında yaşlandırılması ile elde edilmiştir. Bu jel de yine döndürerek kaplama yöntemi ile 3000 rpm’de 3 dk boyunca döndürülerek altaş üzerine film olarak biriktirilmiş ve hava atmosferinde 500°C’de tavlanmıştır. SEM resimlerine göre, yaşlandırılmış jelden elde edilen filmin yüzeyi diğerine oranla daha pürüzsüzdür. Bunun altında yatan sebebin, bu numunedeki boğçalanmış “rod”ların daha küçük boyutlara sahip olduğu düşünülmektedir. Tavlanmış film ise, yine düzlemsel büyümüş, aynı uzunlukta ancak biraz daha dar (210 – 340 nm arasında) ve daha pürüzsüz yüzeye sahip nanorodlardan oluşmaktadır. XRD analizine göre; ısıtım işlemi uygulanmış film de kristal yapıya sahiptir. Çözeltinin yaşlandırılması ile birlikte ısıtım işlemi gerek kalmadan kristalin film elde edilmiştir.





## 1. INTRODUCTION

Most of technological advance depends on the evolvement of the material science. In fact, prehistoric ages such as Stone Age, Bronze Age, Iron Age, and Steel Age are called as materials names. Progression from one of those ages to an upper era was on account of the discovery of a carbonaceous material with higher energy as a source of combustible material as a reducing agent for metals. The beginning to understand of the relations between structural characteristics of materials and their properties, which is obtained over the last two centuries, has authorized us to substantially modify and product characteristics of materials. Thereby, tens of thousands of different materials have evolved with specialized properties to meet our modern society, and correspondingly industrial, automotive and information revolution which was appeared with the quantum mechanics have been seen. Thus, it is obvious that the civilizing process of the humankind has been intimately tied to the capability of processing materials to fill needs [1].

Recent decades, a remarkable effort has been spent to overcome challenges especially including economical and efficient solar cells, batteries with longer life and more capacity, cleaning water, energy saving, efficient catalysts to produce essential chemicals, sensing applications, and capturing CO<sub>2</sub> and other contaminants in air. Nano and thin-film science and technology are responding to such challenges by designing and fabricating superior and multifunctional materials and material systems optimized for energy and environmental applications [2-3].

Vanadium oxides are one of the most widely studied materials on account of having a great potential interest for all those applications due to their superior physical and chemical properties. Such great interest drawn to vanadium oxides is based on two main factors, namely the variety of vanadium oxidation states, ranging from V<sup>2+</sup> to V<sup>5+</sup>, and the variability of oxygen coordination geometries implying octahedral, pentagonal bipyramids, square pyramids, and tetrahedral, which can be combined by shared corners, edges and faces, yielding an impressive variety of structural and crystallographic arrangements. Besides, in particular, such specific properties as a

certain change in physical properties of some V-O system ( $\text{VO}_2$ ,  $\text{V}_2\text{O}_3$  and  $\text{V}_2\text{O}_5$ ) by an external stimulus, layered structures of some vanadium oxides, exhibiting thermoelectric effects, chromogenic characteristics etc. make them fabulously interesting materials [4-15].

Amongst all vanadium oxides,  $\text{V}_2\text{O}_5$  has been extensively studied due to its low cost, rich abundance and the ease of synthesis as a research object of various theoretical and applied studies, such as photocatalysis, solar cells, gas sensors, supercapacitors, and electrochromic devices [16 - 20]. Moreover, the layer structure of  $\text{V}_2\text{O}_5$ , which results in high lithium ion intercalation- deintercalation capability up to three lithium ions per  $\text{V}_2\text{O}_5$ , having relatively high theoretical capacity about  $294 \text{ mAh g}^{-1}$ , and high stability make the structure one of the most-attractive cathode material among rechargeable lithium ion batteries [21].

Nanofibers of various oxides with composite, core/shell, or hollow structures have been produced by customizing the spinning parameters of the electrospinning apparatus [22-23].  $\text{V}_2\text{O}_5$  nanofibers are firstly produced by Kim (24) et al. via electrospinning method by spinning a sol-gel solution containing a solute polymer (poly- (vinylpyrrolidone), PVP), which is followed by annealing at a certain temperature. Afterwards they have been generated as a single-crystal, polycrystalline, and amorphous so far.

Vanadium oxides have been prepared by using a wide range of techniques such as pulsed laser deposition (PLD), electron/ion beam evaporation, magnetron sputtering, spray pyrolysis, chemical vapor deposition, and sol-gel deposition [25 - 30]. Sol gel process is superior over those of other methods in virtue of its versatility and cost effectiveness for a large-scale production. Vanadium oxide gels are prepared by following mainly two routes; an inorganic process that involves acidification and polymerization of decavanadic acid of metal salts in aqueous solution by the help of an ion-exchange resin, and an organic route containing hydrolysis and polycondensation of metal-organics in organic solvents [31 - 32]. Both routes have disadvantageous such as, some chemical species from the ion exchange resin remains in the sol and organovanadium compounds are expensive. An alternative technique to obtain a precursor gel is to react  $\text{V}_2\text{O}_5$  powder directly with diluted  $\text{H}_2\text{O}_2$  solution leading to peroxovanadate sol, which is followed by heating the sol to let polycondensation occur [33]. Prepared sol-gels are employed to produce thin films by

using the methods of spin coating, dip coating, or electrodeposition, while spin-coating is more beneficial compared to dip-coating method due to the higher orientation of molecules during spinning. Passerini et al. [34] found that the insertion capacity of spin-coated films is twice as much as that of dip-coated films have. The properties of vanadium oxide produced by the spin coating technique highly depend on its microscopical and morphological characteristics such as roughness, structure, thickness, crystallinity, which is altered by changing the aging time, annealing temperature, drying temperature, evaporation rate, relative humidity, precursor type, spin-coating rate and time, and even chemical structure of the substrate.

$V_6O_{13}$ , a mixed valance oxide of  $V^{5+}$  and  $V^{4+}$ , has a layered monoclinic structure similar to  $V_2O_5$  but more regular. Although  $V_6O_{13}$  has a very similar structure, it is metallic at room temperature unlike  $V_2O_5$ , which is a wide gap semiconducting. There had restricted exploration on  $V_6O_{13}$  due to the complexity of vanadium-oxygen system, however, it has lately been studied intensively thanks to the improvement in production techniques. It has been studied largely as a potential cathode material for lithium ion batteries due to its layered structure. It has so far been found that as many as six lithium ions are inserted per  $V_6O_{13}$  unit, leading to a very high capacity around 310 mAh  $g^{-1}$ .  $V_6O_{13}$  have been fabricated by thermal decomposition, plasma enhanced chemical vapor deposition (PECVD), and hydrothermal synthesis [35 - 36].

Concordantly, nanofibers, nanorods, 2D-porous structured thin films and thin films with smooth surface produced by a facile wet-chemical method. Spin coating and electrosinning techniques were used to deposit samples from a solution containing polyvinylpyrrolidone (PVP) or an inorganic gel prepared by polycondensation of  $V_2O_5$ - $H_2O_2$  solution. In addition, to the best of our knowledge, it was the first time that crystalline  $V_6O_{13}$  is deposited via sol-gel process. In the end, optical and morphological properties of the produced oxides were investigated by bright field transmission electron microscopy (BF-TEM), selected area electron diffraction (SAED), X-ray powder diffraction (XRD), scanning electron microscopy (SEM), UV-Visible spectroscopy (UV-Vis.), temperature dependent UV-Vis., cyclic voltammetry (CV) and electrochemical impedance spectroscopy (EIS).



## 2. THEORETICAL PART

### 2.1 Vanadium

Vanadium was firstly discovered in 1801 by a Spanish-Mexican mineralogist Andres Manuel del Rio while he was working on a specimen from brown lead ore,  $Pb_5(VO_4)_3Cl$  (Figure 2.1). However, the element he found was erroneously assumed as an impure sample of chromium. 30 years after del Rio, in 1831, Nils Sefstorm, a Sweden scientist, was re-discovered the element second time. Sefstorm chose a name starting with “V” since the letter had not been assigned for any element yet. He named the new element “vanadium” referring to the Scandinavian goddess of beauty and fertility Vanadis (Freyja) due to the wide range of beautifully colored compounds produced by vanadium. The lead mineral that found by del Rio was then renamed vanadinite for its vanadium content. The pure vanadium was obtained for the first time by Henry Enfield Roscoe by reducing vanadium(II) chloride,  $VCl_2$ , with hydrogen, in 1867. Vanadium, for the first time, was used industrially in the steel alloy chassis of Ford Model T, in 1905, along with facilitated reduced weight meanwhile remaining tensile strength [37 - 40].

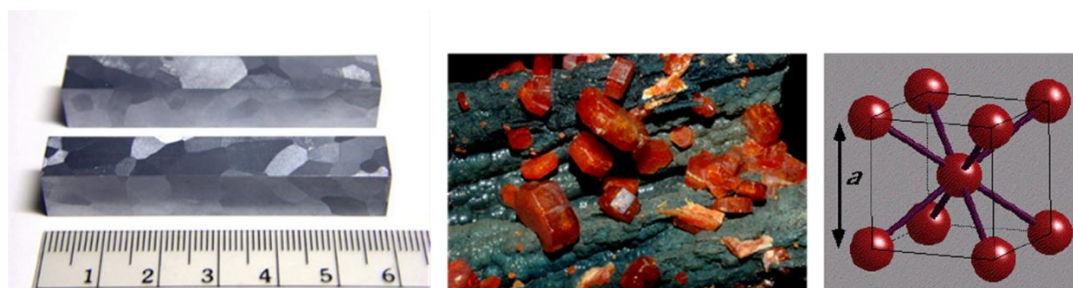


**Figure 2.1 :** Free vanadium metal (left), vanadinite (middle), and a presentation of crystal structure of vanadium, BCC (right) [41].

Vanadium occupies about 200 ppm (0.02%) of the lithosphere and it is the 22nd most abundant element of the earth crust. It occurs in 65 varied minerals, while pure metallic vanadium is rare in nature. Patronite ( $VS_4$ ), carnotite ( $K_2(UO_2)_2(VO_4)_2 \cdot 3H_2O$ ), and vanadinite ( $Pb_5(VO_4)_3Cl$ ) are economically the most important minerals of vanadium.

Metallic vanadium, which has a body-centered cubic crystalline cell, is silvery grey, harder than most of metals and steels while ductile, and malleable. However, a small

amount (100 ppm) of hydrogen absorption embrittle the vanadium metal. It has a good corrosion resistance against saltwater, air, sulfuric acid ( $\text{H}_2\text{SO}_4$ ), hydrofluoric acid (HF), hydrochloric acid (HCl), and alkalis at room temperature. It oxidizes with air/oxygen at about  $660^\circ\text{C}$  and the most stable oxide of the vanadium,  $\text{V}_2\text{O}_5$ , is formed, an oxide layer which prevents the metal against further oxidation is formed even at room temperature though.

Vanadium is a d-transition metal in the 4<sup>th</sup> period and Group V-B on the periodic table of the elements. The abbreviated ground state electronic configuration for vanadium is  $[\text{Ar}] 3d^3 4s^2$  which means valence electrons of vanadium are located as 2 electrons on 4s sub-shell and 3 electrons on 3d sub-shell. As a result of the partially filled 3d shell of vanadium, it includes multiple oxidation states, varying from +2 to +5, which can be distinguished by their colors. In aqueous solution of vanadium, which usually prepared with ammonium metavanadate ( $\text{NH}_4\text{VO}_3$ ), metal aquo complexes of which the colours are lilac  $[\text{V}(\text{H}_2\text{O})_6]^{2+}$ , green  $[\text{V}(\text{H}_2\text{O})_6]^{3+}$ , blue  $[\text{VO}(\text{H}_2\text{O})_5]^{2+}$ , and yellow  $[\text{VO}(\text{H}_2\text{O})_5]^{3+}$ , where the oxidation states of vanadium are respectively +2, +3, +4, and +5, are formed as seen in Figure 2.2.



**Figure 2.2 :** Aqueous solution of +2, +3, +4 and +5 ions of vanadium [42].

## 2.2 Vanadium-Oxygen System

Since vanadium has multiple oxidation states, varying from +2 to +5, it has various oxide forms. The principal oxides of vanadium are VO,  $\text{V}_2\text{O}_3$ ,  $\text{VO}_2$  and  $\text{V}_2\text{O}_5$  that occur as single valency oxides in the oxidation states of  $\text{V}^{2+}$ ,  $\text{V}^{3+}$ ,  $\text{V}^{4+}$  and  $\text{V}^{5+}$ , respectively. In addition of these oxides, vanadium-oxygen system also includes

mixed valency oxides, containing two oxidation states together in an oxide form. For instance,  $V_8O_{15}$ ,  $V_7O_{13}$  and  $V_6O_{11}$  are between  $VO_2$  and  $V_2O_3$ , containing  $V^{3+}$  and  $V^{4+}$  species, meanwhile  $V_6O_{13}$  is with  $V^{4+}$  and  $V^{5+}$  species. These mixed-valance oxides are categorized with related stoichiometries, such as Magnéli phases which are formulated as  $V_nO_{2n-1}$  (including  $V_3O_5$ ,  $V_6O_{11}$ ,  $V_7O_{13}$ ,  $V_8O_{15}$  etc.), and Wadsley phases with the formula of  $V_{2n}O_{2n+1}$  ( $VO_3$ ,  $V_6O_{13}$  etc.). The formation of the mixed-valance oxides is associated with the oxygen vacancies. If the number of oxygen vacancies exceeds a certain value, the vacancies tend to correlate and form the so-called crystallographic shear planes, i.e. the vacancies associate along a lattice plane and become subsequently eliminated by reorganization of V-O coordination units [11].

The crystalline characteristics and the properties of the vanadium oxides change according to their vanadium/oxygen ratio. Each oxide has its own characteristic. For instance, at room temperature, VO has a cubic (rocksalt) crystalline structure and metallic-grey color,  $V_2O_3$  has a monoclinic structure, black color and shows antiferromagnetic properties, while  $VO_2$  occurs in a tetragonal rutile structure, has a dark-blue color and shows diamagnetic properties. Some basic properties of vanadium oxides are listed in Table 2.1.

**Table 2.1** : Some properties of single-valance vanadium oxides.

Oxide	Color	Oxidation State	$T_{SMT}$ (°K)	Crystal Structure	Magnetic Structure
VO	Metallic grey	$V^{2+}$ (3d3)		Cubic (rocksalt)	Magnetic
$V_2O_3$	Black	$V^{3+}$ (3d2)	160	Corundum (at 25C), monoclinic ( $T < T_c$ )	Antiferromagnetic ( $T_N=168K$ )
$VO_2$	Dark blue	$V^{4+}$ (3d1)	340	Monoclinic (at 25C), rutile ( $T > T_c$ )	Diamagnetic
$V_2O_5$	Yellow to brown	$V^{5+}$ (3d0)	530	Monoclinic (at 25C), layered orthorhombic	Diamagnetic

In terms of crystallinity, the V-O system is so complicated that contains 13 distinct solid crystalline phases with countless chemical compounds as seen from Figure 2.3. These crystalline phases are:  $\alpha$  (body centered cubic),  $\beta$  (body centered tetragonal),  $\gamma$  (monoclinic),  $\delta$  (face centered cubic, i.e. halite),  $\delta'$  (body centered tetragonal, i.e.  $V_{52}O_{64}$ ),  $V_2O_3$  (corundum),  $V_3O_5$  (monoclinic), Magnéli phases  $V_nO_{2n-1}$  where  $n=4, 5$ ,

6, 7, and 8 (triclinic),  $\beta$ -VO<sub>2</sub> (tetragonal),  $\alpha$ -VO<sub>2</sub> (monoclinic), V<sub>6</sub>O<sub>13</sub> (monoclinic), V<sub>3</sub>O<sub>7</sub> (monoclinic) and V<sub>2</sub>O<sub>5</sub> (orthorhombic) [43 – 44].

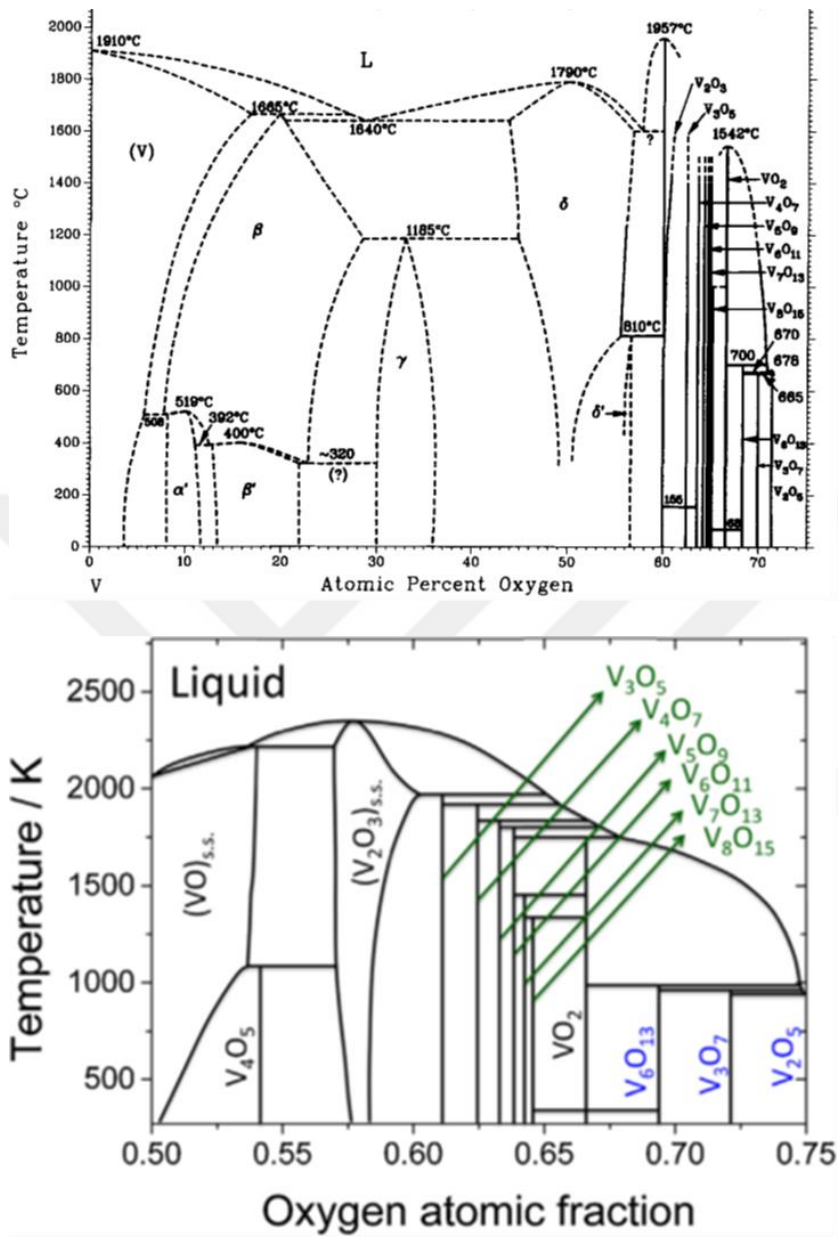


**Figure 2.3** : Vanadium-oxygen phase diagram; the whole range (top), and low oxygen content (bottom) [44 - 45].

Some oxide forms of vanadium exhibit semiconductor to metal transitions (SMT) (also called as metal-insulator transition, IMT or MIT) at a respective temperature,  $T_{SMT}$ . These vanadium oxides having SMT are semi-conducting with relatively low electrical conductivity below  $T_{SMT}$  and show a transition into a metallic state at  $T_{SMT}$ . The SMT is a first order phase transition and reversible. During SMT, all atoms relocate at the same time to form a new crystalline structure with redistribution of electronic charge and hence the nature of interaction changes. As a consequence, materials exhibit a

distinct change in their characteristics such as electrical, magnetic and optical properties. The SMT of vanadium oxide, increases with the oxygen ratio of O/V, i.e., the higher oxidation state of the vanadium atom of the compound, the higher  $T_{SMT}$ , as seen from Table 2.1. Among vanadium oxides exhibiting SMT,  $VO_2$  is one of the most studied materials because it has a  $T_{SMT}$  at  $340^\circ K$  which is near the room temperature, while  $V_2O_3$  and  $V_2O_5$  undergoes SMT at  $160^\circ K$  and  $530^\circ K$ , respectively.  $VO_2$  and  $V_2O_3$  have monoclinic phase below  $T_{SMT}$ , and  $V_2O_5$  is orthorhombic, while their crystalline phases differ from these structures with a change in electrical conductivity up to 10 orders of magnitude above  $T_{SMT}$ . The change in conductivity for some materials having SMT are given in Figure 2.4 [46].

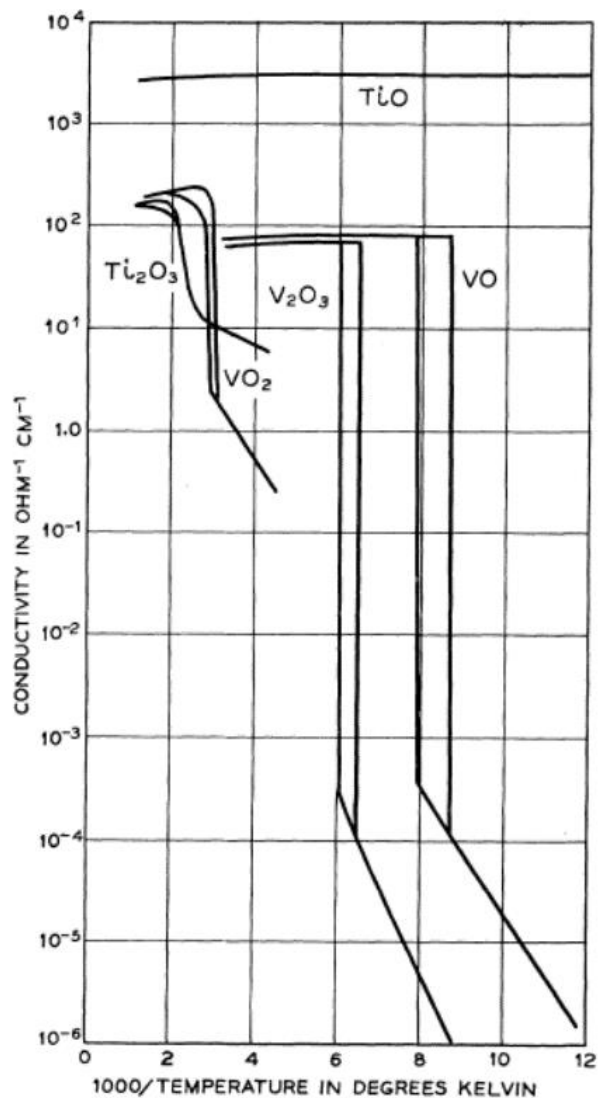


**Figure 2.4 :** The change in conductivity versus reciprocal temperature for some materials exhibiting SMT [47].

Several vanadium oxides are chromogenic materials whose color change reversibly by an external stimulus such as temperature (thermochromism), electronic charge-discharge (electrochromism), electromagnetic radiation (photochromism) and a gas atmosphere (gasochromism). These chromogenic characteristics make vanadium oxides excellent candidates for such applications that sensors, energy saving smart windows as coatings, and switching devices.  $\text{VO}_2$  and  $\text{V}_2\text{O}_3$  exhibit good thermochromism in thin film forms. When they are applied onto a smart window, they are transparent in the infrared region under  $T_{\text{SMT}}$  and undergo opaque at  $T_{\text{SMT}}$ , while no transparency change in the visible range.

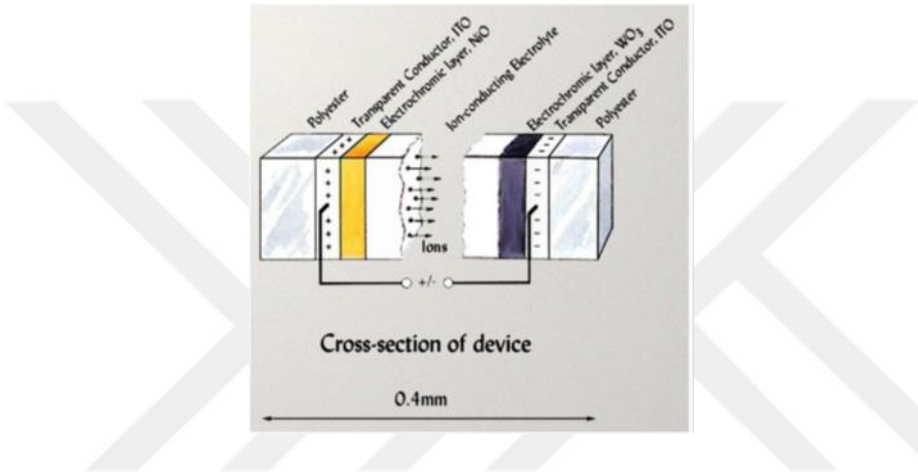


**Figure 2.5 :** Sketch of an EC device, showing typical materials and the movement of ions [48].

$\text{VO}_2$  and  $\text{V}_2\text{O}_5$  has reversible and persistent electrochromic properties. When a charge is applied, their color change until the charge is extracted again.  $\text{V}_2\text{O}_5$  has an exceptional electrochromic characteristic since it exhibits both anodic (coloring upon electrochemical oxidation) and cathodic (coloring upon electrochemical reduction) electrochromism, while  $\text{VO}_2$  has only anodic electrochromism.  $\text{VO}_2$  and  $\text{V}_2\text{O}_5$ , as electrochromic materials, have usage in four main applications; smart windows, information displays, variable emittance coatings and variable reflectance mirrors.

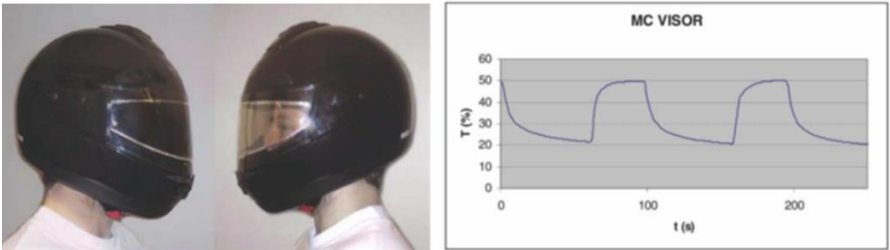
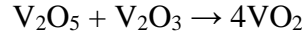


**Figure 2.6 :** Switchable motorcycle helmet visor made. The spectra (right) shows the change in visible properties with an applied voltage of 1.6 V [49].

### 2.2.1 Vanadium(VI) oxide, VO<sub>2</sub>

Vanadium(IV) oxide, so-called as vanadium dioxide (VO<sub>2</sub>), is a dark blue solid and synthesized by synproportionation of vanadium(III) oxide (V<sub>2</sub>O<sub>3</sub>) and vanadium(V) oxide (V<sub>2</sub>O<sub>5</sub>);



It is a strongly correlated material with d1 electron system and well known to have four polymorphs, including VO<sub>2</sub>(A), VO<sub>2</sub>(B), VO<sub>2</sub>(M1) and VO<sub>2</sub>(R). While these polymorphs has the same formula, VO<sub>2</sub>, their crystalline and electronic structure are completely different and highly complex. They exhibit many attractive properties due to strong correlation effect, and thus this characteristic makes VO<sub>2</sub> one of the most attractive material among vanadium oxides. VO<sub>2</sub>(R) has a tetragonal rutile structure, which is the most stable phase of VO<sub>2</sub>, while VO<sub>2</sub>(M1) has a monoclinic structure that is the result of the distortion of the metallic rutile VO<sub>2</sub>(R) phase. The other polymorphs VO<sub>2</sub>(A) and VO<sub>2</sub>(B) have tetragonal and V<sub>6</sub>O<sub>13</sub>-like layered monoclinic structures, respectively.

The reason behinds the fact that VO<sub>2</sub> is the most studied solid-state thermochromic material is VO<sub>2</sub> undergoes SMT at near room temperature around 340°K with an abrupt and large change in transmittance of infrared radiation. The T<sub>SMT</sub> of VO<sub>2</sub> can be even decreased by doping or some thermal or electrical treatments. Above T<sub>SMT</sub>, VO<sub>2</sub> is in the tetragonal rutile form VO<sub>2</sub>(R), where the tetragonal lattice VO<sub>6</sub> octahedral are elongated slightly along fourfold axis. VO<sub>2</sub> turns to monoclinic structure VO<sub>2</sub>(M1) where the VO<sub>6</sub> octahedral are more severely distorted if the temperature is decreased under T<sub>SMT</sub>. Both structures include the adjacent octahedral units connected by edges or corners as seen in Figure 2.7.

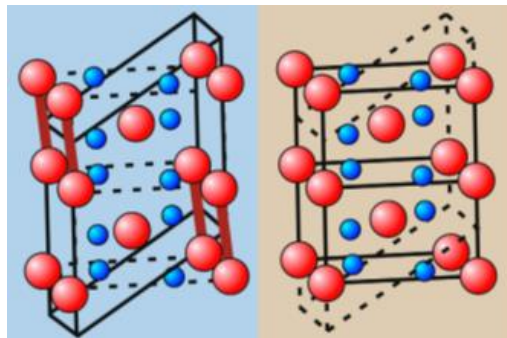


**Figure 2.7** : Comparison of the crystal structures of VO<sub>2</sub>(M1) (left) and VO<sub>2</sub>(R) (right). Red balls represents vanadium atoms, while blue balls are oxygen atoms [50].

VO<sub>2</sub>(R) and VO<sub>2</sub>(M1) are the most studied VO<sub>2</sub> polymorphs, while monoclinic VO<sub>2</sub>(B) phase has also been explored. However, most of these researches have focused on the layered structure of VO<sub>2</sub>(B) with an open framework, which is the result of the edge-sharing VO<sub>6</sub> octahedral. Since layered structure lets more ions insert the material, this characteristic makes VO<sub>2</sub>(B) an attractive intercalation material for electrochemical applications. However, it is hard to produce single crystalline VO<sub>2</sub>(B) because of the complex crystal structure. The tetragonal VO<sub>2</sub>(A) is the least studied phase among VO<sub>2</sub> polymorphs because of the limited synthesizing of pure crystalline phase by the complexity of the crystal phases of VO<sub>2</sub> alike VO<sub>2</sub>(B). The complexity of crystal structure of VO<sub>2</sub> is composed of the narrow range of phase diagram as seen from Figure 2.8, and the instability of the polymorphs thermodynamically. VO<sub>2</sub>(A) and VO<sub>2</sub>(B) are metastable in bulk form and turn irreversibly into VO<sub>2</sub>(R) when heated, resulting in a mixture crystalline structure of polymorphs. The formation of that mixture phase limits studying the properties of these polymorphs. Therefore, VO<sub>2</sub>(A) and VO<sub>2</sub>(B) have not been explored well in terms of their properties and so possible usage for applications.

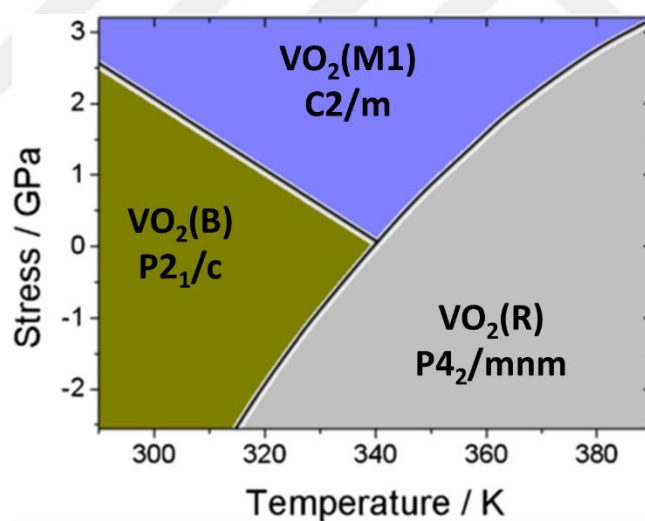


**Figure 2.8** : Schematic phase diagram of VO<sub>2</sub> [45].

### 2.3 Thin Film Production Methods

Properties of the fabricated films are related to their structural and crystallographic characteristic, which highly dependent on both the fabrication method and parameters applied before and after the production.

### **2.3.1 Chemical vapor deposition**

Chemical vapor deposition is one of the oldest method to produce thin films. The first practical use was seen in the development of incandescent lamps in the 1880s. The metal or carbon coating process applied to increase the strength of the filament in the lamp is the first known application of this method.

Chemical vapor deposition processes is a method to obtain a solid film as a product by reacting the precursors of the gas phase under appropriate conditions.

In CVD process, there are many factors that affect the coating properties such as type, size and shape of the vacuum chamber, gas flow rate, alignment. Generally, low and high temperature are classified and categorized according to various conditions such as low and high pressure, cold and hot wall, open and closed system. There are basically three elements that should be in a CVD system; a controller that provides control and conduction of the initial components that will enter the vacuum chamber, an energy source that will conduct the chemical reaction, and a discharge system that will remove the produced and consumed gases from the vacuum chamber.

Plasma enhancing chemical vapor deposition is a method in which CVD is deposited on a substrate by plasma generation using a substrate reactive gas. Plasma is formed by two electrodes, usually RF, DC or microwave discharge, placed in the gap where reactive gases are present. There are many interchangeable parameters in the PECVD system to ensure high quality and reproducibility of plasma formation. External parameters include pressure, gas flow, discharge excitation frequency, power; Electron density, electron energy distribution function, electrical potential are called internal parameters. In this system, an electric power is applied at a high voltage at a low pressure. As a result, the gas breaks down and the plasma containing electrons, ions and excited atoms is obtained. Steam reactors electron collisions are ionized and dissociate. Thus, chemically active ions and radicals undergo chemical reaction at or near the surface of the material. Subsequently, thin film deposition occurs.

### **2.3.2 Physical vapor deposition**

The physical vapor deposition method is a thin film deposition technique in which the target material in a solid state is deposited on a substrate by converting the target material into a gaseous phase in a vacuum environment at low pressure. Generally, this method is used to make coatings varying from 1 nm to 1  $\mu\text{m}$ . With this method, it

is possible to produce multi-layered and very thick coatings. In the physical vapor deposition method, a coating rate of 1-10 nm/sec is generally used. This method is divided into two basic groups as evaporation and sputtering according to the method of vapor formation. The evaporation method is based on heating the target material to the vapor phase. The splashing method is based on the physical collision process in which the kinetic energy is transferred onto the target material. The electron beam evaporation method is a physical vapor deposition method in which accelerated electrons bombarded onto a target material by an electron source are accumulated on the substrate material by passing the heating target material through the vapor phase to the vapor phase. With this method, it is possible to vaporize ceramics, glass and metals with a high melting temperature. In this method, a high current is passed through the filaments to warm the filaments to high temperatures. At these temperatures high-energy electron beams are produced from the filaments. These electron beams are accelerated by applying high voltage (10-20 kV) and are focused on the target material to be evaporated by the magnetic field. These high-energy electron beams focused on the target material allow the target material to melt and evaporate or directly sublime. A thin film is produced by accumulating the target material passing into the vapor phase on a substrate. By using the electron beam and physical vapor deposition method, it is possible to produce thin films with pore-free and non-porous thin films depending on the angle made by the substrate material of the vapor arrival angle, by rotating the substrate material at a certain speed

Sputtering is the process of breaking atoms and molecules from target material with energetic particles. The broken particles reach the substratum and perform the plating process. The magnetron sputter method is designed to allow more intensive material breaking. In fact, similar physical phenomena occur with the standard sputter process. There are magnets in the magnetron sputter source to enhance the plasma. At the source, there is a neutral electrode on the outside and a negative electrode on the middle (where the target is located). The sputter process gas used is generally argon (Ar). The argon has a large atomic weight and preferably does not react with any material. The Ar atom colliding with a free electron in the medium ionizes and becomes  $\text{Ar}^+$  and strikes the target material on the negative electrode due to the influence of the electric field. During this process, the electron belong to the Ar atom ionizes other Ar atoms, thus forming a plasma environment. The magnets, which are

placed opposite to each other in the center of the sputter source and magnetized to the magnetron, strengthen the electrons intensively in the region on the target by means of the magnetic field lines they create, so that the plasma strengthens in this region. In this region where the plasma is dense,  $\text{Ar}^+$  ions break down atoms (or molecules) from their surface by transferring electrical energy to the momentum they acquire by the target material. These broken particles move with their initial velocities towards the substrate and other directions. The atoms that come to the substrate surface are nucleated here to form the film.

Shortly sputtering process, energetic ions formed in a plasma in front of a target (or cathode) plate bombard this target. Thus, by bombardment, the target atoms are torn away or splashed. These atoms then accumulate on a substrate (the surface to be coated) as a thin film. As a consequence of ion bombardment, secondary electrons are also emitted from the target surface, and these electrons play an important role in sustaining the plasma

### **2.3.3 Wet-coating (sol-gel)**

The sol-gel method is a method based on hydrolysis and condensation reactions of starting solutions such as metal alkoxide and inorganic salt. Although the sol-gel method is quite expensive and troublesome, some advantages of this method play a major role in the production of nanoparticles. These advantages can be summarized as the ability to produce materials from minerals and chemicals in a controlled manner at the desired size and shape, with molecular markers homogeneously developed process steps. However, the biggest drawback is that the amount of product obtained is very small compared to the input product, which means that the efficiency is very small, except that the system is expensive and troublesome. In addition to nanoparticle production by sol-gel method, it is also preferred for production of dense materials, fibers and thin film surface coatings, powder, coating and fiber production. The schematic representation of the production of these materials by the sol-gel method is shown in Figure 2.9.

The sol-gel method is a very useful method for making ceramics and glassware. Generally, in the sol-gel process, the system migrates from the liquid phase (sol) to the solid phase (gel). With this method, it is possible to produce many ceramic and glass materials. These; very pure and spherical powders, thin film coatings, ceramic fibers,

microporous inorganic membranes, monolithic ceramics and glass, or highly porous aerogel materials.

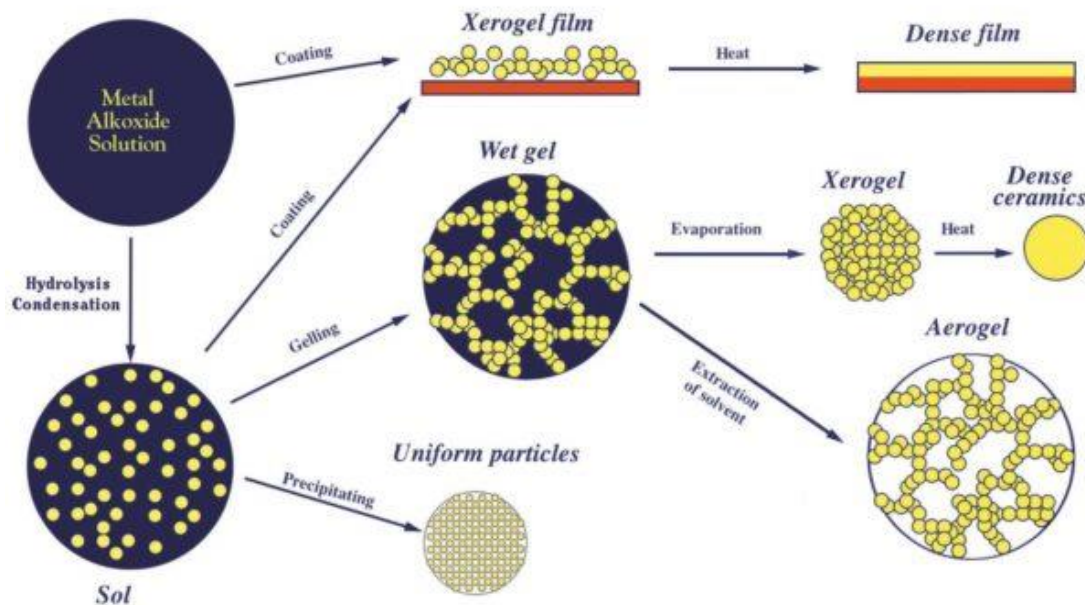


**Figure 2.9 :** Schematic illustration of the preparation of various kinds of materials by sol-gel method [51].

Starting materials for the sol are inorganic metal salts or metal inorganic compounds. In a typical sol-gel process, the base material is dissolved in the solvent and converted to a sol, which is a colloidal structure with a series of hydrolysis and polymerization reactions. Colloidal structures are between heterogeneous and homogeneous structures. Although the solved particles are not very small particles, they do not collapse but do not separate from the solvent. Ceramic materials can be produced in different forms at the end of the processes on the "sol".

Thin films are produced by coating the "sol" on a substrate with spinning, spraying, and dip coating methods. The sol will turn into a wet gel (xerogel) when coated on this substrate. Then the thin film will come to the foreground by applying the temperature and drying it into dense gel (Figure 2.9).

The sol-gel method has many advantages. The tools and materials used in this method are very simple. The thickness of the films obtained by this method is the same all over the surface and a pure coating is obtained. It saves energy, does not interfere with the prepared environment, and can be coated on materials with all kinds of geometric shapes by this method. Another important advantage is that the microstructure of the coated film is easily controllable. With this method, it is possible to make films with

low refractive index because porous structure can be obtained. However, there are some disadvantages besides these advantages. Some of those; the cost of the material is excessive and material loss during coating is high. In addition, the chemicals used can be harmful to your health.

Components used in the sol-gel method are;

- Metal oxides: They are used as the starting material to form the sol. (H) methoxyl, (O) ethoxyl.
- Catalysts: Materials that do not participate in any reaction but increase the reaction rate. There are two types of catalysts, acidic and basic.
- Alcohols: Used to dissolve metal oxides. The solvent is selected according to the nature of the oxide. Ethyl alcohol (ethanol), propyl alcohol is used as the starting material in methanol sol-gel method and reacts with metal oxides.

### **2.3.3.1 Electrodeposition**

Electrochemical deposition is the depositing process of solid particles with a thin layer by electrolysis onto a material (electrode) surface. The purpose of this process is to change or improve properties such as surface appearance or corrosion resistance. Electrochemical deposition is required electrically conductive materials such as metals, alloys, semiconductors and conductive polymers to be coated.

Electrochemical deposition is carried out in a solution called electrolyte or coating bath. This electrolyte is often an ionic solution in which the material is dissolved to be coated on the surface. The material is immersed to be coated in the solution and connected to the power supply so that the cathode can function. In order to complete the electric circuit, an electrolyte is connected to an anode. The power supply provides the current required for plating. The positively charged metal ions in the solution move toward the negatively charged cathode, where they are reduced to become metallic and cover the surface of the material.

### **2.3.3.2 Dip-coating**

Dip Coating is a method of coating by submerging and withdrawing a substrate at a controlled rate in atmospheric conditions and under controlled temperatures. During the immersion, the bottom layer should be smooth and smooth. Thin and smooth

coating depends on a smooth surface, minimum vibration of the underlayer and correct speed control. The coating thickness is mainly defined by the traction speed, the thickness of the layer and the fluidity of the liquid.

In coatings made with solvents such as alcohol, there is no need for filtration. A boundary layer is formed which contains the ‘sol’ side of the coating area in accordance with the mechanism of the carrier in motion, the fluids when sole is immersed. The boundary referred to in the coating and draining phase is divided into two layers, the inner layer and the outer layer. As the inner layer moves with the carrier, the outer layer moves in the opposite direction and returns to the sole.

Filming thickness depends on the severity of the main stream that separates the layers moving up and down. The principal forces in the film formation are as follows; The force of gravity of the upwardly moving carrier to the fluid, the force of gravity, the inhale surface tension to hold the carrier, the ‘sol’ moment of inertia reaching the coating area, and the separating or binding pressure.

$$t = c\left(\frac{\eta v}{\rho g}\right)^{1/2} \quad (2.1)$$

Where;

$\eta$ : Viscosity of the liquid,

$v$ : Velocity of the substrate,

$g$ : Gravity acceleration,

$c$ : Rate constant, and

$\rho$ : Density

### **2.3.3.3 Spin-coating**

Spin coating has been used for the last few decades to produce very thin films and relatively thick films on flat substrates. Various materials such as semiconductor solutions, polymers and some organics are successfully coated on metal, plastic, glass and semiconductor substrates for different purposes. In this technique, the material to be coated naturally must be dissolved in a liquid solvent. Typically, the substrate to be

coated is held on a rotating platform with the aid of a motor and the coating solution is applied manually or with the automatic arm to the substrate. The substrate is rotated at very high angular speeds (300 to 10000 rpm) to ensure that the solution is uniformly distributed over the surface of the substrate. The resulting film thickness can be successfully formed from 30 nm to several microns per layer. The theory behind this coating technique is based on the equilibrium between the viscous forces determined by the viscosity of the liquid with the centripetal force that the rapid transformation forms. The film thickness can be adjusted by controlling the rotation speed, the speed and the viscosity of the solution. Significant advantages of spin coating are reproducibility, obtaining homogeneous films, simplicity, ease of integration, application on different substrates and low cost. The main disadvantage of this technique is the necessity to use smooth and smooth surfaces.

#### **2.3.4 Electrospinning**

Electrospinning method enable to produce polymeric surfaces starting from a few microns in diameter and consisting of nanofibers ranging in diameter up to 100 nm.

Electrospinning is a technique in which electrical forces are applied to obtain polymer nanofibers. The method of electrospinning was first discovered by Rayleigh in 1897. The first registered patents on the production of nanofibers by the electrostatic method were taken in 1902. In 1934, Anton Formhals further developed the method and received a new patent. In 1960's various studies by Taylor, the basic theoretical principles of electrochemistry were explained. In one of these studies, it was shown that the cone interface between the two liquids is balanced within the electric field. Under the influence of the electric field, the surface of the liquid is loaded and an external force is generated by mutual forces pushing each other. After passing the threshold value, with electrostatic force, the liquid droplet assumes a conical shape and overloads exit the charged jet formed at the tip of the cone. Taylor explains that the cone is formed at this critical point where the electrical force equals the surface tension. The patented viscosity of the solution, dielectric coefficient, conductivity and volatility characteristics are the basic parameters of the electro-spinning method.

Basically, to perform electrospinning process with polymer solution, there are three component that are the high-voltage power supply, feeding unit and the collector (conductive plate). The polymer solution is poured into the syringe solution and

exposed to the electric field. When the electrical field is applied, the electrical forces act in opposition to these two forces. This electrical charge separation produces an effect that counteracts the surface tension of the feed solution. As jet move away from Taylor Cone surface, it gain speed and axial movement. This allows the jet to be stretched. When the electric force exceeds the surface tension force, the droplets are separated by the jets and move toward the collector. The number of jetting on the surface of Taylor Cone increases with increasing voltage. During jet formation, the solvent is removed. In this way, the nanofibers can be collected in dry form on the collector plate. As a result, fibers are formed in the collector plate at diameters ranging from 3 nm to 1 micron.

#### **2.3.4.1 Electrospinning parameters**

Parameters affecting electrofiber drawing method: solution variables (molecular weight, molecular weight distribution, structure of polymer, solution properties, viscosity, conductivity, surface tension, elasticity, etc.), process parameters, applied voltage, hydrostatic pressure in capillary tube, flow Speed, distance between collector and syringe barrel, plate movement) and environmental variables.

The shapes and dimensions of the fibers depend on a large set of parameters, such as molecular weight, molecular weight distribution, glass transition temperature, viscosity, viscoelasticity, concentration, surface tension, and electrical conductivity. These are called as solution parameters.

The concentration of the solution in the electrospinning method determines whether fiber from solution can be produced or not. The solution concentration at which the electrical force is applied in the optimal range. If the solution concentration is too low or too high, no fiber can be produced. The minimum solution concentration is required for the fiber formation. Generally, when other factors are kept constant, the increase in solution concentration causes an increase in fiber diameter. However, increase of the concentration must be in the range where the surface tension can be renewed by applying overvoltage.

Solvent has an important effect on electrical and rheological properties such as molecular weight, conductivity, dielectric constant, surface tension and viscosity. High molecular weight polymers affects fiber morphology in electrospinning process. Thus, this is preferred in electrospinning method because they provide the desired viscosity

for fiber production. When polymers having very low molecular weight are used in the electrospinning process, they are more prone to pilling in fiber production. The average diameter of high molecular weight solution is effective in producing larger fibers.

Viscosity is measure of the resistance of a fluid against flow under surface tension. The solution viscosity affects the morphology and fiber diameter of the polymeric fiber during electrospinning. Optimum viscosities are required in the electrospinning process since fiber production is continuously not possible in very low viscosity solutions, and in the case of very high viscosity solutions, it is difficult to feed the polymer solution. Researchers have reported that the highest electrostatic viscosity value is between 1 and 215 poise. The increase in solution viscosity or concentration brings about more uniform and large diameter fiber production.

Surface tension play a critical role for fiber formation in the electrospinning method by reducing the surface tension of the nanofiber solution with solvent. Different solvents can provide different surface stresses. Generally, very high surface tension of the solution stops the electrospinning process due to jet irregularity and droplet production. The formation of fiber, droplets and beads depends on the surface tension of the solution, and the lower feed solution helps to electrostatically apply lower voltage.

The solution conductivity is required for fiber formation because electrospinning method is based on the transmission of electrical charges from the primary electrodes to the supply solution. For this reason, it is not possible to produce nanofibers by this method from solutions when an electrical conductivity is value of "0". The solution conductivity value is specified by Siemens (S) unit and is 1 Siemens = 1 Ampere/Volt.

The charged ions in the polymer solution are effective in jet formation. The solution conductivity is usually determined by the type of polymer, the solvent used and the ionisable salts. Natural polymers such as gelatin are usually present in the form of polyelectrolytes in nature. Increasing the solution conductivity to a certain level provides finer nanofiber formation. It is not possible to produce nanofibers with a conductivity value greater than 5 mS/cm<sup>2</sup>.

One of the most effective parameters in the electrospinning method is the applied voltage to the feed solution. Fiber production begins with the exceeding of the threshold voltage in the electrospinning method. The applied voltage ensures that the

solution is loaded with electrical charges during the electrospinning process. As the voltage increases, the surface charge come out on the electrospinning jet, the solution is loaded more charge, the jet length is increased and a more unstable structure is gained. For this reason, increases with the applied voltage leading generally to smaller fiber diameters.

The feed rate determines how much polymer solution is converted to nanolife unit time. The flow rate should be equivalent to the amount of polymer solution moving from the feed point to the plate. Otherwise, the formation of nanofibers does not occur with a continuous and proportional nanofiber diameter distribution. Taylor Cones do not occur in low debris, whereas in high debris, nanofibers are formed in droplet with large diameter value. The high flow rate Taylor Cone "also reduces the electrical loading. As a result, there is an increase in the diameter of the nanofibers or the formation of the nanofibers completely.

Collector plate type is parameter affecting geometrical shape and morphology of the produced nanofiber. When the nanofibers come into contact with the grounded collector plate, their electrical charges left on surface. These affect the density of the nanofiber morphology, especially in the unit area. For this reason, the dielectrical properties of the material from which the collector plate is produced are important. The collectors of the devices used in laboratory conditions generally consist of fixed metal plates. There are also studies in the literature with rotary cylinders, rotary plates, wire frames in various geometrical shapes, ring shaped electrodes and reciprocal cone collectors. The collecting geometries determine how the nanofibers are collected and the moving collectors provide the nanofiber accumulation at the desired density in the unit area.

The distance between the feeder and collector plate determines how strong the electrical field is and how long the solvent in the solution will travel away from the nanofibers. When other conditions are kept constant, the increase in distance causes a decrease in the diameter of the nanofibers in general. However, in some cases it has also been observed that the opposite is. Also, distance between collector plate and feeder affects the morphology of the fiber as much as the fiber diameter. It should be value of the distance to get the solvent away from the nanofiber jet. Otherwise, the nanofibers accumulate in the form of age and form on nanofiber. The short formation

of the distance also leads to the instability in the Taylor Cone and consequently the formation of defective morphological structures.

Ambient conditions such as temperature, humidity of the environment affects the evaporation time of the solvent in the solution during the electrospinning process. These conditions must be checked to obtain dry fiber. In general, with the circulation of heated air at temperatures of 25 – 57 °C, and in devices with extra heat source, the evaporation of the solvent in the formation of the jet takes place more rapidly.





### 3. EXPERIMENTAL PART

#### 3.1 Reagents and Substrate Preparation

All chemicals were reagent grade and used as received without further purification. The production of the VO<sub>x</sub> nanofibers and thin films comprised commercial vanadium(V) oxide powder (V<sub>2</sub>O<sub>5</sub>, %99.6, Aldrich, USA), diluted 30% hydrogen peroxide solution (H<sub>2</sub>O<sub>2</sub>, Merck, Germany) and polyvinylpyrrolidone (PVP, Mw = 1.300.000, Sigma, USA). Acetone, ethanol and distilled water were used to clean substrates. The electrolyte used for electrochemical characterization was involved anhydrous lithium perchlorate (LiClO<sub>4</sub>, 95.0%, Alfa Aesar, Germany) and propylene carbonate (C<sub>4</sub>H<sub>6</sub>O<sub>3</sub>, 99.0%, Alfa Aesar).

The substrate chosen is so important for thin film technology. It is used as a mechanical supporter and withal as insulator or conductor in electronic applications. Substrates should have those characteristics;

- mechanically strong,
- lack of chemical reactivity,
- providing a good adsorbtion for the film,
- a smooth and clear surface.

To prevent the formation of defects or inhomogenities in the produced film, the defiled surface of the substrate material should be cleaned well. Thus, substrates were cleaned with detergent and flushed with copious amounts of deionized water firstly. Afterward, they rinsed in acetone and ethanol mixture in ultrasonic cleaner for 10 minutes. Ultrasonically cleaned substrates then washed with ethanol and deionized water, subsequently, and finally dried in air at room temperature.

Various substrates depend on the requirements of the characterization technique were used in this study for thin film deposition. Microscope slides (2947, 75x25 mm, Corning, USA), which made from soda lime glass, were used as substrate for optical characterization since they have

a high transmittance in the 300 to 500 nm range, and structural characterization as their surfaces are highly smooth. In addition, unpolished indium doped tin oxide glasses (ITO), ( $\text{SnO}_2\text{:In}$ , CG-50IN-CUV, 7x50x0.7 mm, Delta Tech., USA), indium tin oxide coated polyethylene terephthalate films (ITO-PET), (639303, Aldrich), steel and aluminum plates were used as substrates for electrochemical characterization.

### 3.2 Solution Preparation

The reaction of  $\text{V}_2\text{O}_5$  in concentrated  $\text{H}_2\text{O}_2$  is highly exothermic and dangerous since the liquid bubbles noisily and overflows from the vessel, and the condensation occurs in a few minutes. In order to control the gel formation and avoid the danger, a series of solutions with lower  $\text{H}_2\text{O}_2$  content were prepared. After finding the exact concentration of  $\text{H}_2\text{O}_2$  for a safe experiment, a series of trials were done to find-to-find the maximum  $\text{V}_2\text{O}_5$  powder that the diluted  $\text{H}_2\text{O}_2$  solution can solve. At the end, a more diluted  $\text{H}_2\text{O}_2$  solution (wt. 3%) which prepared from the 30% solution by adding distilled water has been used.

Three different solution preparation route were followed:

- i. A 0,1 gr of  $\text{V}_2\text{O}_5$  powder was added to 4 ml of 3%  $\text{H}_2\text{O}_2$  in an open vessel to let oxygen that produced as result of the reaction leave the system, and mixed for an hour to produce a dark red solution. Then, 0,35 gr of PVP was added into that solution with rapid agitation and stirred for 2 hours. The end solution is named as Sol-A.
- ii. In the second route, 0,1 gr of  $\text{V}_2\text{O}_5$  powder was added to 4 ml of 3%  $\text{H}_2\text{O}_2$  and mixed for an hour. Then the solution was heated at  $80^\circ\text{C}$  for an hour to produce a highly viscous dark red gel as a consequence of the polycondensation of the solution by the hydrolysis of vanadium species with air. The final viscous gel is called as Sol-B.
- iii. For the last route, a Sol-B gel was aged for 10 days in a sealed vessel under room conditions to see the effect of the aging time on morphological and electrochemical characteristics of the film. This gel is named as Sol-C.

The preparation routes of the solutions Sol-A, Sol-B and Sol-C are represented in Figure 3.1.

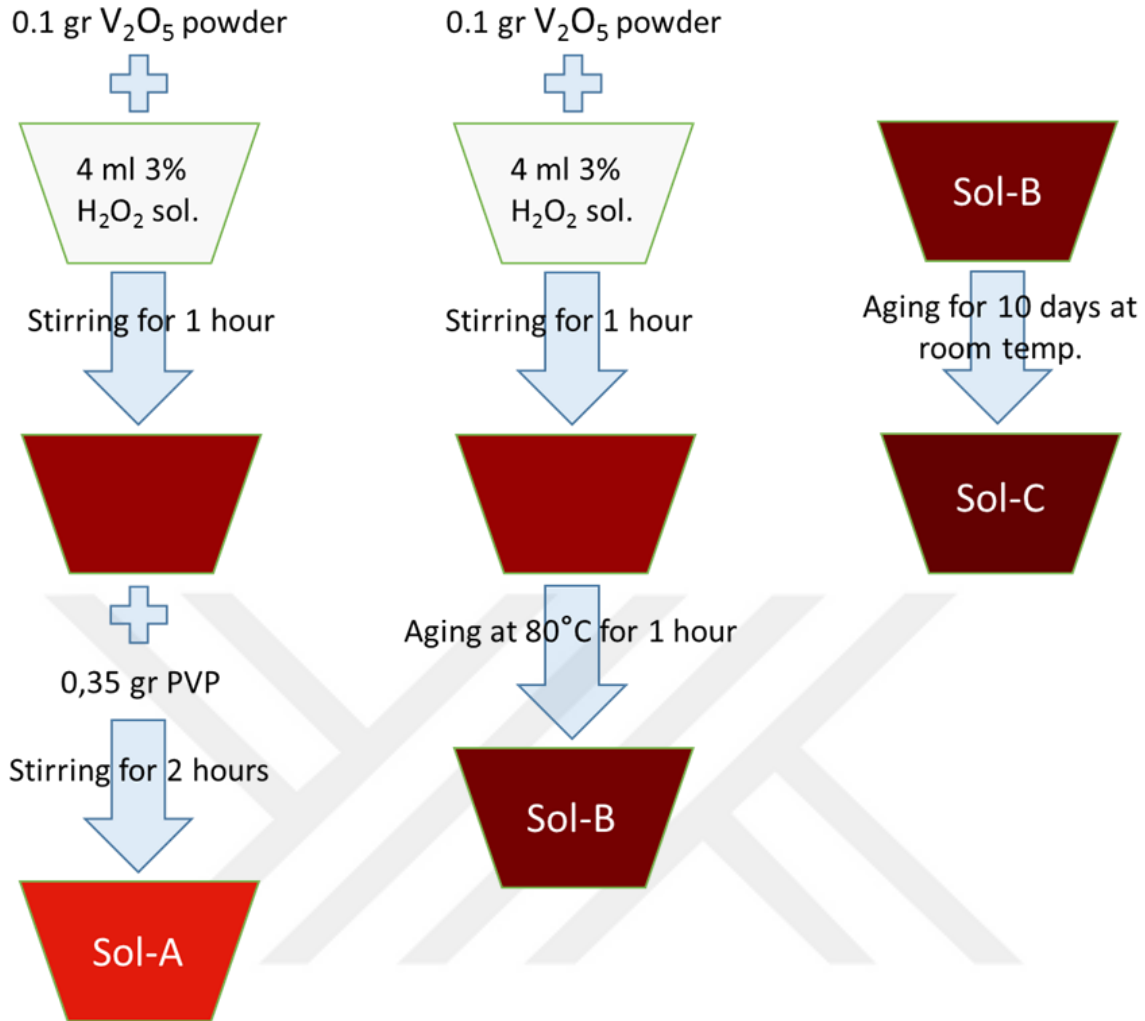


**Figure 3.1** : A schematic representation of the preparation of solutions.

### 3.2.1 Solution Characterization

Optical properties of the prepared solutions were examined by transmittance and absorbance measurements in the range of 300-900 nm of wavelength in a quartz cell, which is chosen to avoid cell absorption in the UV range, by a spectroscopy system (Agilent HP-8453 model UV/VIS spectrophotometer).

It found that Sol-B and Sol-C were almost fully opaque within the whole range, while the optical properties of Sol-A were changing in time. The transmittance of Sol-A was increasing in the process of the time as shown in Figure 3.1. However, it was almost constant after a while. It can be dedicated that the Sol-A is not stable. The absorption edge of the Sol-A is at about 520 nm and no change is observed over time.

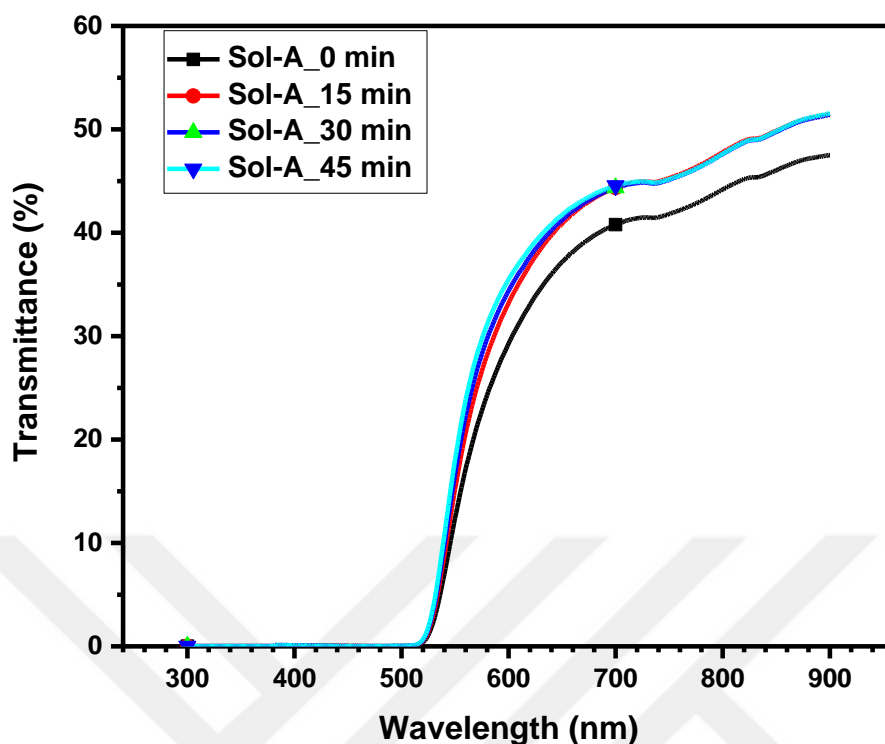


**Figure 3.2** : UV-visible spectra of the Sol-A at different times.

Conductivity measurement of the solutions were performed by using a conductometer (WTW LF95, Germany) at room temperature. The probe of the conductometer was separately dipped in the solutions and waited for 5 minutes in case the probe was wetted completely by each solution. It was carefully cleaned with ethanol and distilled water before using for the next solution.

The surface tensions of vanadium solutions were measured by a tensiometer (Dataphysics DCAT 11EC, Germany) by the Wilhelmy plate method at room temperature. Dataphysics SCAT the software was used to evaluate the results that were obtained from the tensiometer.

The viscosity values of the solutions were found by a rotational rheometer (Haake Rheostress 1, Germany) using the plate-plate sensor (dia 35 mm, gap 1 mm) configuration at 25°C. The shear rate range was in between 0 and 300 s<sup>-1</sup> in 150 s as shown in Figure 3.3. Since solutions were not Newtonian fluids, a software (Haake RheoWin3 Data Manager, Germany) were used to model the obtained results according to the power-law equation:

$$\tau = K\dot{\gamma}^n \quad (3.1)$$

where;

$\tau$  is the shear stress (Pa),

$K$  is the consistency index (Pa.s),

$n$  is the flow behavior index (-) and

$\dot{\gamma}$  is the shear rate ( $s^{-1}$ ).

Calculating  $K$  and  $n$  values in the equation, the apparent viscosity (Pa.s) can be computed using the power-law equation for viscosity:

$$\eta = K\dot{\gamma}^{n-1} \quad (3.2)$$

The maximum shear rate for a Newtonian fluid flowing in a tubular geometry can be found from the following equation:

$$\dot{\gamma}_{max} = \frac{4Q}{\pi R^3} \quad (3.3)$$

where  $Q$  is the volumetric flow rate, and  $R$  is the inside radius of the tube.

It can be modified for a non-Newtonian fluid by inserting  $\dot{\gamma} = f(\sigma) = (\sigma/K)^{1/n}$  into the equation as:

$$\dot{\gamma}_{max} = \left[ \frac{3n + 1}{4n} \right] \left[ \frac{4Q}{\pi R^3} \right] \quad (3.4)$$

During the electrospinning process, the solution were fed at a rate of 1.5 mL/h, which can be re-expressed as  $4.17 \times 10^{-10} \text{ m}^3/\text{s}$ . The radius of the tip where the solution whipped into the electric field was about 0.4 mm ( $0.4 \times 10^{-3} \text{ m}$ ). On the other hand, samples were coated by spin coating method at the spinning rates of 1500 and 3000 rpm.

After  $n$  values were determined (Table 3.1), by using Eqn. 3.4, maximum shear rate of the electrospun solution was calculated as  $8.296 \text{ s}^{-1}$ , while, the maximum shear rate of spin-coated samples were found as  $1.5708$  and  $3.1416 \text{ s}^{-1}$  for 1500 and 3000 rpm, respectively. According to Eqn 3.1, the apparent viscosities of the solutions were found as  $0.0378 \text{ Pa.s}$  for electrospun Sol-A,  $0.0477 \text{ Pa.s}$  spin-coated Sol-A,  $8.99$  and  $16 \text{ Pa.s}$  for spin coated Sol-B and Sol-C, respectively.

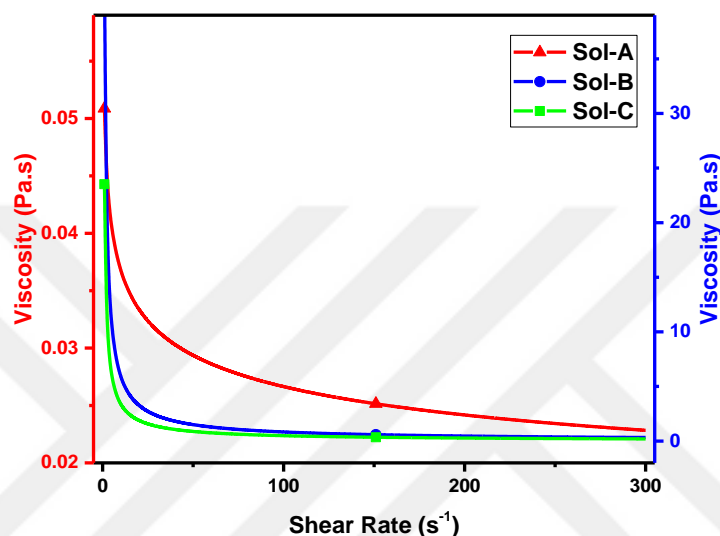


**Figure 3.3 :** Viscosity values versus shear rates of the prepared solutions. Right y-axis gives the viscosity value of Sol-B and Sol-C.

The measured properties of the solutions are listed in Table 3.1. In the table,  $\eta$  represents the viscosity value, while ES and SC written below represent electrospinning and spin coating, respectively. It is clearly seen that the aging time influences the properties of the gel. As the gel is aged, a sharp difference in its surface tension and viscosity values is observed. The viscosity of the gel increases, while its surface tension decreases. However, its conductivity increases slightly with aging.

**Table 3.1 :** The measured properties of the solutions.

Solution	Conductivity (mS/cm)	Surface Tension (mN/m)	K (Pa.s <sup>n</sup> )	n (-)	$\eta_{ES}$ at $8.296 \text{ s}^{-1}$ , (Pa.s)	$\eta_{SC}$ at $1.5708 \text{ s}^{-1}$ , (Pa.s)	$\eta_{SC}$ at $3.1416 \text{ s}^{-1}$ , (Pa.s)
Sol-A	7	66.1	0.050875	0.85955	0.0378	0.0477	-
Sol-B	2.63	40.4	23.515	0.16	-	-	8.99
Sol-C	2.85	26.5	42.595	0.14485	-	-	16

### 3.3 Nanofiber and Thin Film Deposition

The Sol-A solution containing PVP was put into a syringe of the electrospinning instrument (NE100, Inovenso, Turkey) equipped with a 0.8 mm gauge electrically conductive brass needle. The distance between the tip of the needle and glass substrates attached on the metal collector was fixed 150 mm. A voltage of 20.3 kV was applied to the needle while the metal collector plate was grounded. The feeding rate of the solution was adjusted at a constant rate of 1.5 ml/h using a syringe pump (New Era Pump Systems Inc., NE-300, USA). Electrospun nanofibers were collected at room temperature on to substrates that were held onto the collector.

Three varied thin films were produced by spin coating method with a spin coater instrument (Inovenso, Turkey) at room temperature:

- i. Sol-A was dropped on substrates and coated at 1500 rpm for 2 minutes (the deposited film is named as SC\_A).
- ii. Since Sol-B was much more viscous compared to Sol-A, the spinning rate was increased to 3000 rpm which was the maximum value of the equipment and Sol-B spinned for 3 minutes on substrates (referred as SC-B).
- iii. Sol-C was coated at the same conditions as Sol-B (the film named as SC-C).

Electrospun nanofibers and produced films were first dried at 80°C for 6 hours and then subsequently annealed at 500°C in a furnace (CWF 110, Carbolite, China) with air atmosphere heated at a rate of 5°C/min for 60 minutes. The produced samples were identified as NF-A500, SC-A500, SC-B500 and SC-C500 while one of each sample were kept without annealing and called as NF-A0, SC-A0, SC-B0, and SC-C0 as listed in the Table 3.2.

**Table 3.2** : List of the deposited samples.

Sample	Solution	Technique	Annealing Temp. (°C)
NF-A0	Sol-A	Electrospinning	No annealing
NF-A500	Sol-A	Electrospinning	500
SC-A0	Sol-A	Spin Coating	No annealing
SC-A500	Sol-A	Spin Coating	500
SC-B0	Sol-B	Spin Coating	No annealing
SC-B500	Sol-B	Spin Coating	500
SC-C0	Sol-C	Spin Coating	No annealing
SC-C500	Sol-C	Spin Coating	500

### **3.4 Electrochemical Characterization**

The electrochemical behavior of the films and nanofibers were examined by a potentiostat/galvanostat (Parstat 2263, AMETEK, USA). The conventional three-electrode cell were used in all electrochemical experiments where VO<sub>x</sub> film or nanofiber deposited on various conductive substrates as the working electrode, Ag/AgCl and Pt wire as reference and counter electrodes, respectively. A 1M solution of anhydrous lithium perchlorate (LiClO<sub>4</sub>) in propylene carbonate (C<sub>4</sub>H<sub>6</sub>O<sub>3</sub>) were prepared ultrasonically in nitrogen atmosphere to use as the electrolyte for the experiments.

The assembled cells were cycled galvanostatically using the potentiostat within and at the potentials of -1.2 and 1.2 V (vs. Li/Li<sup>+</sup>) for cyclic voltammogram analysis at scan rates of ranged from 2 to 50 mV/s.

Electrochemical impedance spectroscopy (EIS) measurements were carried out with the same experimental arrangement. All samples were galvanostatically cycled various times before EIS measurements until equilibrium was established. During the analysis, AC voltage of frequency between 10 mHz and 100 kHz at a scan rate of 10 mV is applied to cells at room temperature. The impedance data of the samples were plotted on the complex plane. Equivalent circuit modelling for the simulation of the EIS spectra of the sample electrodes was performed with ZSimp Win programme (v3.10).

### **3.5 Structural and Morphological Characterization**

The morphological analyses of the nanofiber samples was carried out by scanning electron microscopy (SEM, Zeiss Ultra Plus FE-SEM) operated at 3 kV. Thin film and nanofiber samples fabricated on substrates were hold on carbon tape and coated with gold prior to SEM characterization to prevent charging.

The structure of the SC samples was characterized by Philips CM20 type transmission electron microscope (TEM) operated at 200kV. For the TEM investigations, the layers were removed from the substrate surface by ultrasonic shacking in alcohol and were dripped to a TEM grid with carbon membrane. To evaluate the electron diffraction patterns, the ProcessDiffraction program was used.

The crystallinity of the annealed nanofibers was established by X-ray diffraction (XRD, Bruker Phaser D2 X-ray diffractometer with Cu K $\alpha$  radiation,  $\lambda=1.5418 \text{ \AA}$ ).

Thermochromic properties of the annealed thin film samples SC-A500, SC-B500 and SC-C500 were investigated by PG T80+ UV-Vis spectrophotometer using a spectral bandwidth 0.1 nm in the wavelength range 360-110 nm. A custom-made sample holder heated by cartridge type heaters made of NiCr was used to heat the samples. Cooling of the holder was obtained using a suction air pump. Temperature of the sample holder was controlled and monitored using PtRh–Pt thermocouples. Transmission spectra of the samples were measured at three different temperatures ( $T = 25, 100, \text{ and } 200 \text{ }^\circ\text{C}$ ) to investigate thermochromism in vanadium-oxide thin films. Heating and cooling measurements were repeated for several times for selected samples to test the reversibility of the change in transmittance with changing temperature.



## 4. RESULT AND DISCUSSION

### 4.1 Structural and Morphological Analysis

#### 4.1.1 X-ray powder diffraction characterization

X-ray diffractometer analysis were carried out to examine the crystalline characteristics of the samples. The wide-angle XRD patterns for the amorphous and crystalline vanadium-oxide thin films deposited onto corning glass substrates are shown in Figure 4.1.

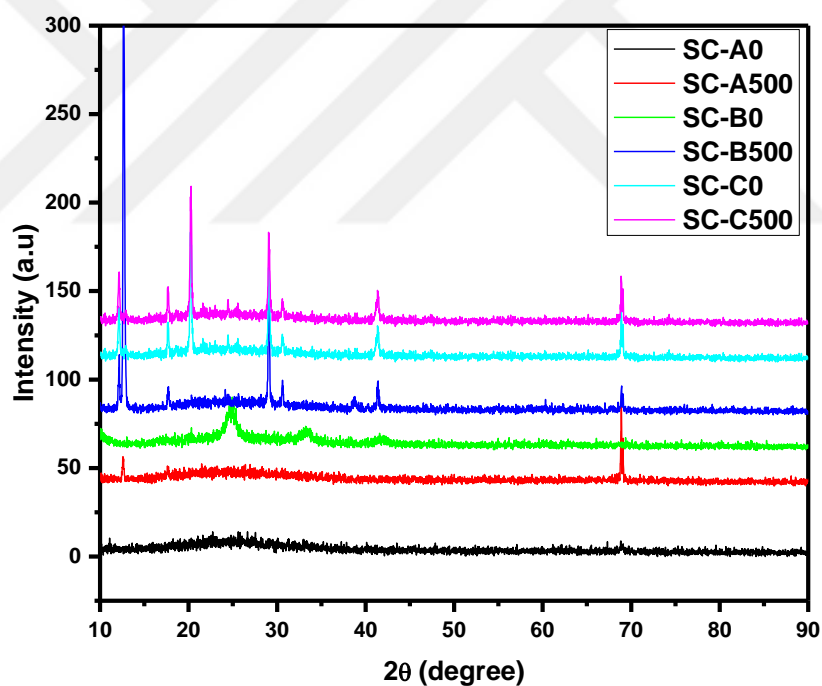


**Figure 4.1 :** XRD patterns of the SC-A0, SC-A500, SC-B0, SC-B500, SC-C0 and SC-C500 from bottom to top, respectively.

The XRD pattern of SC-A0 reveals that the film is amorphous. The thin film partly crystallize after annealed at  $500^\circ\text{C}$ , as seen from the XRD pattern of the SC-A500. It is well known that the existence of a polymer in the solution hinders the crystallization. There are only two peaks seen for SC-A500, which are at  $2\theta$  values of  $12.7^\circ$  and  $69.9^\circ$

and a halo between  $2\theta=16-38^\circ$  values. The spectra are superimposed with the best match to be found in the International Center for Diffraction Data (JCPDS) library of spectra, which was orthorhombic vanadium oxide.

SC-B0 sample exhibits 3 broad peak structures at  $2\theta$  values about  $23.2^\circ-26^\circ$ ,  $32.3^\circ-34.3^\circ$  and  $41.6^\circ$ . These peaks are not well defined so the sample SC-B0 is amorphous. However, after annealing at  $500^\circ\text{C}$ , a small amount of diffraction peaks appear as seen at XRD pattern of SC-B500.

XRD pattern of SC-C0 displays some peaks, which reveals that the sample has crystalline characteristic even without any heat treatment. As comparing patterns of SC-B0 and SC-C0, the effect of the aging of the solution is seen clearly. On the other hand, SC-C500 has same diffraction peaks as SC-C0 with higher intensities. The annealed sample SC-C500 has improved crystalline nature, which is confirmed through the increased intensities of diffraction peaks.

#### **4.1.2 Transmission electron microscopy investigations**

It is hard to define the exact structural characteristic of vanadium oxide because of the complexity of the vanadium–oxygen structure; it is difficult to completely rule out the presence of lower oxides of vanadium in thin films using only XRD studies. Thus, further characterizations were examined by transmission electron microscopy (TEM).

The bright-field (BF) TEM images and the selected area electron diffraction (SAED) patterns from the SC layers are shown in Figure 4.2. The unheated SC-A0 sample was shown to be amorphous by XRD pattern, which was partly confirmed by TEM, as shown in Figure 4.2. Most of the layer is amorphous V-oxide. However, in addition to the amorphous material, a smaller amount of crystalline phases is formed, which assumed to have  $\text{VO}_2$  structure as shown BF image with higher magnified in Figure 4.3. The size and amount of these particles are such that the XRD analyses cannot detect them properly. In the case of non-heat-treated SC-B0 and SC-C0 samples, the situation is similar. The layers are XRD amorphous because crystalline V-oxide particles of the samples cannot detect due to their small size. For existence of these crystalline phases can be inferred from the SAED patterns shown in Figure 4.2.

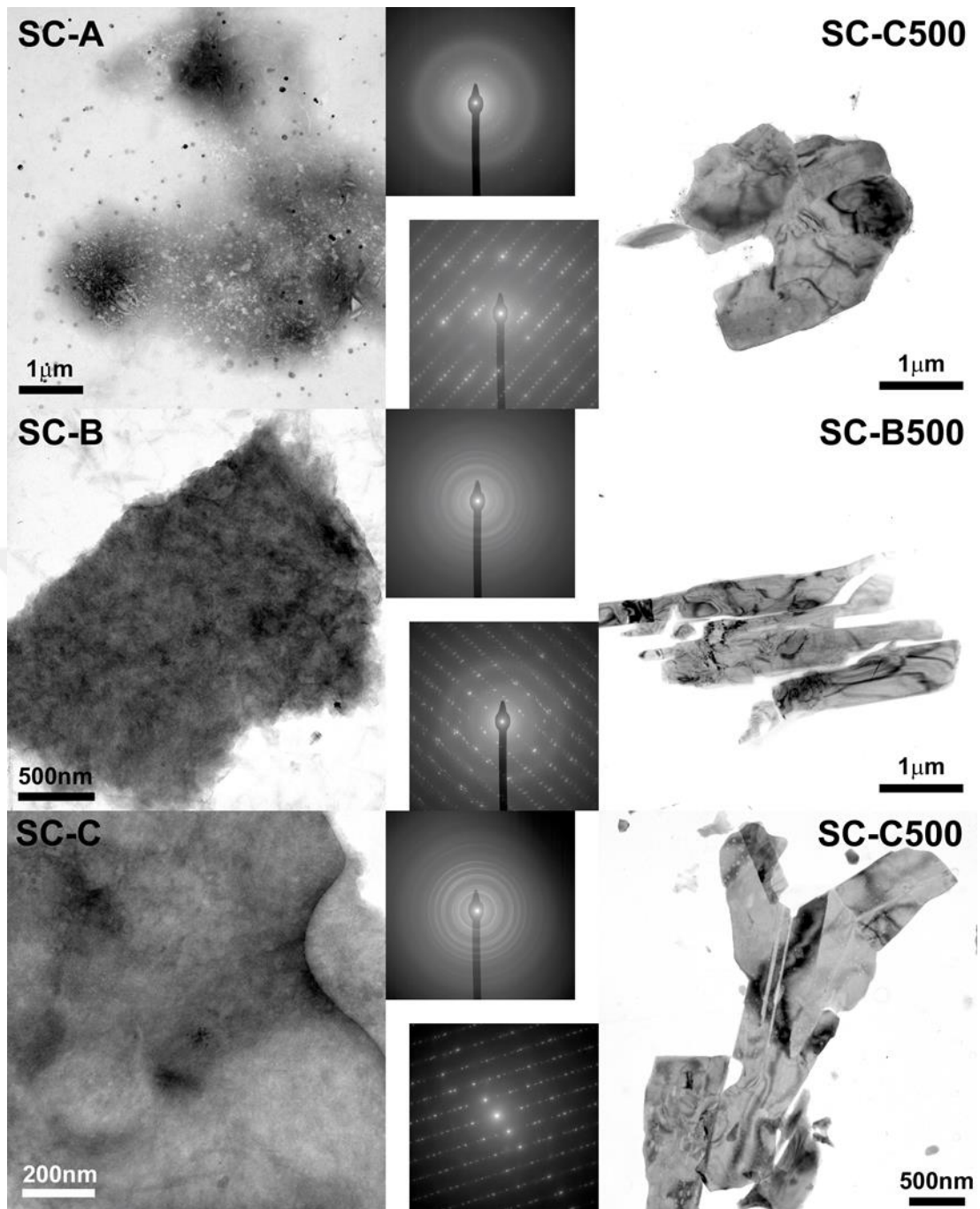


**Figure 4.2 :** The BF-TEM images and SAED patterns of the SC samples.

After heat treatment at 500°C, very similar layers are formed in the SC-A500, -B500 and -C500 samples. That plate grains are formed with 2-5 μm size, there structure can be V6O13 (monoclinic, cell parameters:  $a = 1.1911$  nm,  $b = 0.3674$  nm,  $c = 1.013$  nm,  $\alpha = 90^\circ$ ,  $\beta = 100.9^\circ$ ,  $\gamma = 90^\circ$ ) based on the SAED patterns (Figure 4.3), but it is assumed that the particles structure is not clearly determined due to the complexity of V-oxide, probably other V-oxide phases were also formed in the V6O13 grains. On the SC-A500 sample, grains are more irregular than those found in SC-B500 or SC-

C500, or some of them may be horseshoe as shown in Figure 4.2. In the SC-B500 and SC-C500 samples, the flakes have a more regular shape and are needle-like. The flakes are mostly made up of a large crystal, possibly with twin boundaries. Lighter patches are particularly visible in the grains, as shown in a higher magnification BF-TEM image of the SC-C500 sample in Figure 4.3. The appearance of patches on the SC-C500 sample is common, where it can be found on each particle, the size of the patches ranges from 10 to 100 nm in this sample. Patches can be caused by impurities or structural changes in the flakes that may explain extra reflections observed on the SAED patterns.

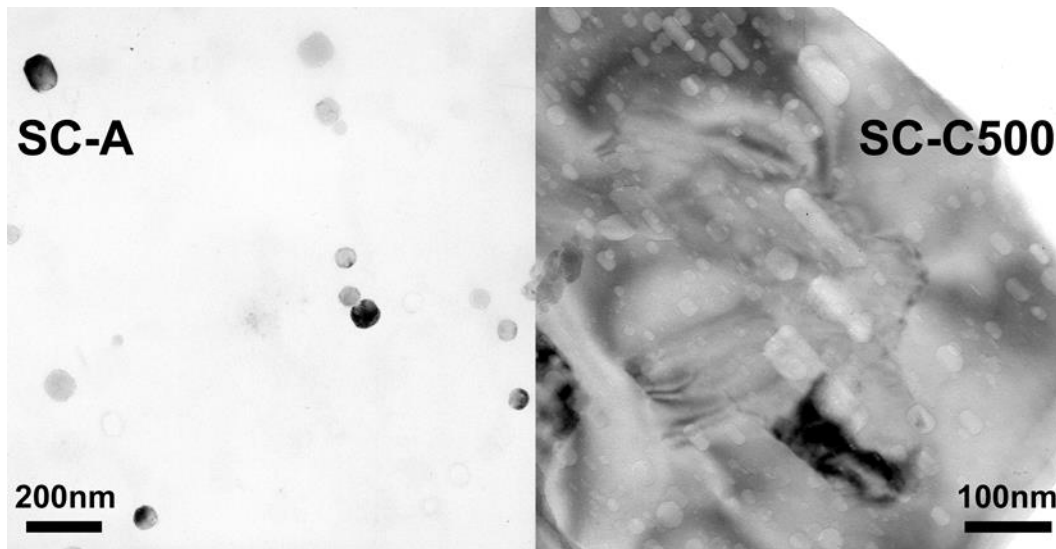


**Figure 4.3 :** BF-TEM images at higher magnification from the nano crystals weakly presented in the SC-A and from the precipitations observed in the SC-C500 (lighter quadrilateral in the sheet grain).

The average intensity over circles in the function the scattering vector based on the polycrystalline SAED pattern of the SC-A0, SC-B0, SC-C0 and SC-C500 samples can be seen in Figure 4.4. Accordingly, the weakly presented crystalline phases in the unheated SC-A0 layer are likely to be  $\text{VO}_2$  phase (tetragonal , cell parameters:  $a = 0.2851 \text{ nm}$ ,  $b = 0.4552 \text{ nm}$ ,  $c = 0.4552 \text{ nm}$ ,  $\alpha = 90^\circ$ ,  $\beta = 90^\circ$ ,  $\gamma = 90^\circ$ ), where it should be taken into account that these particles are in special orientation so they are textured as shown in the BF-TEM image in Figure 4.3, while the non-heat-treated SC-B0 and SC- C0 samples may be consisted of  $\text{V}_6\text{O}_{13}$  phases. However, not all the peaks were identified on the diffraction patterns, which suggests that other V-oxide structure can be presented in the samples.

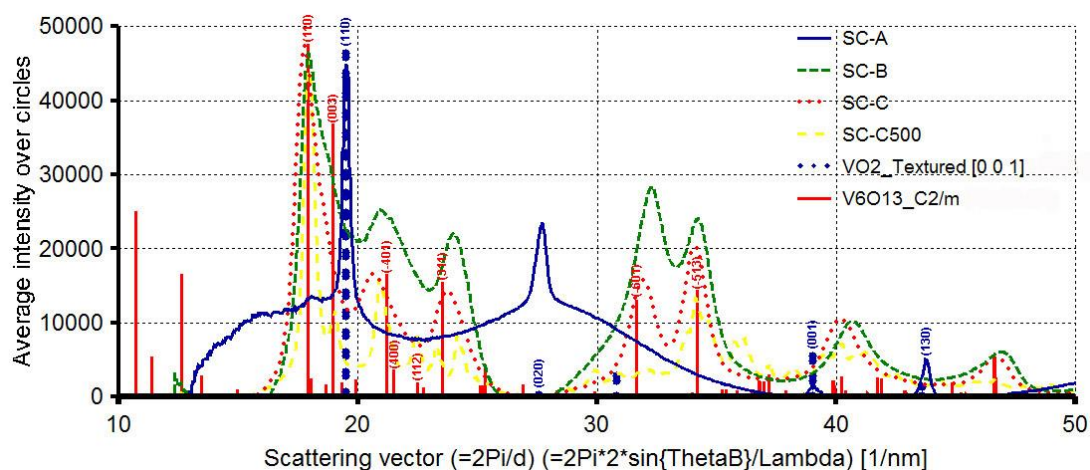


**Figure 4.4 :** The average intensity over circles in the function the scattering vector based on the polycrystalline SAED patterns of the SC-A, SC-B, SC-C and SC-C500 samples. The perpendicular lines indicate the locations of the  $V_6O_{13}$  structure and the [001] textured  $VO_2$  structure, based on XRD data.

#### 4.1.3 Surface morphology by scanning electron microscopy

Morphological and microstructural characteristics of prepared samples have been investigated by scanning electron microscopy. SEM images of the electrospun sample NF-A0 are given in Figure 4.2. It can be clearly seen from the images that nanofibers were deposited concentratedly. Nanofibers have smooth and uniform surfaces, high aspect ratio, and uniform diameter in the whole range. Moreover, beads and some relatively bigger droplets present diffusely. The basic reasons underlying behind the bead formation is that the viscosity of the solution at low PVP concentration is relatively lower than the surface tension. Thus, the surface tension becomes dominant, the whipping jet tend to decrease its surface area, and so bead formation is observed. Besides, charge density is another factor of the bead formation. It is well known that the bead formation is more easily occurs as the fiber diameter decreases. Therefore, to obtain bead free nanofibers with very thin diameter is very hard. According to Figure 4.2, the fiber diameter ranges from 15 to 240 nm. The average fiber diameters were found to be  $59.1 \pm 40$  nm that is undoubtedly very thin, while beads were formed as a matter of course.

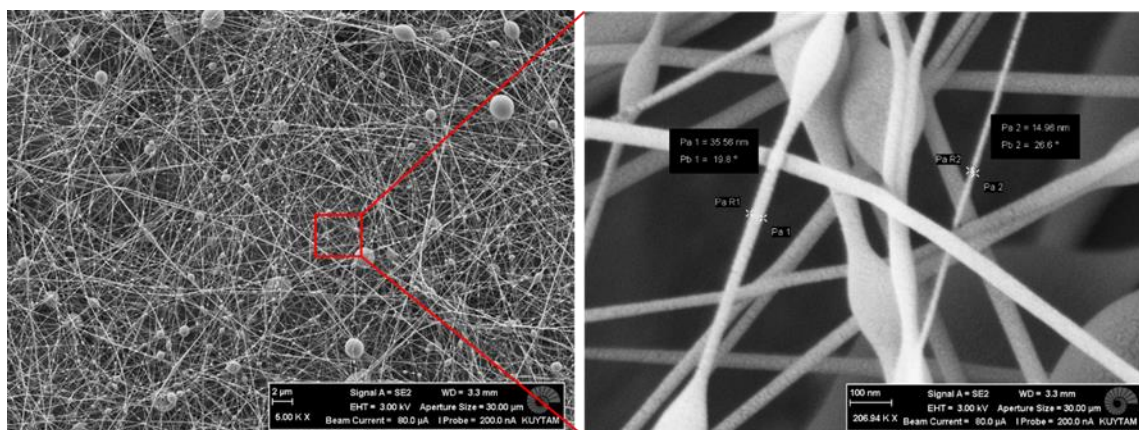


**Figure 4.5 :** SEM micrographs of NF-A0.

SEM images of electrospayed sample that annealed at 500°C are shown in Figure 4.3. Well-grown  $V_2O_5$  nanorods with smooth surfaces in a grassland-like nanoarchitecture are clearly observed. The width and length of the nanorods were confirmed to be approximately 250 to 640 nm and 1 to 5  $\mu\text{m}$ , respectively. Moreover, there are few nanowire-like 1D nanostructures. The formation of these 1D structures is expected because of the presence of some thick nanofibers before annealing.

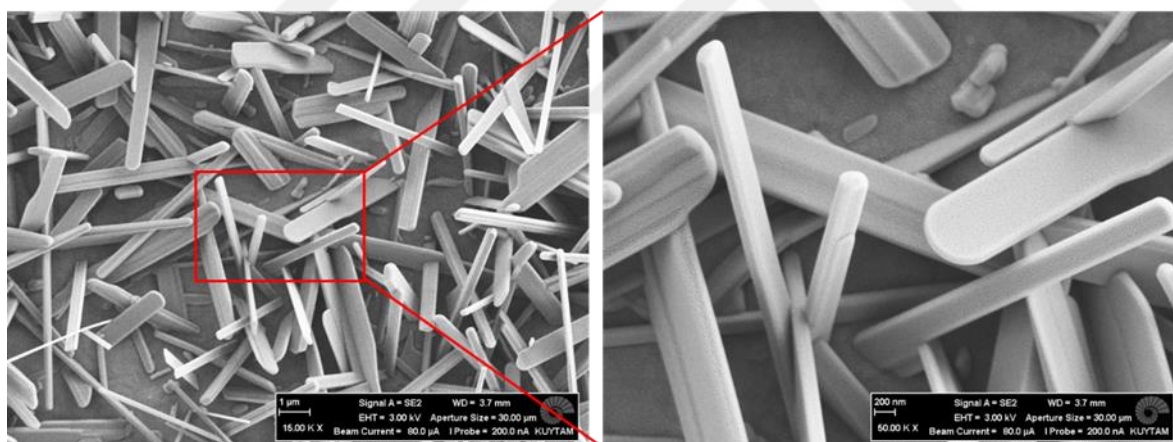


**Figure 4.6 :** SEM micrographs of electrospayed films that annealed at 500°C.

SEM micrographs of SC-A0 and SC-A500 prepared by spin coating of Sol-A are given in Figure 4.4. It can be clearly seen from the images that uniform surface of SC-A0 containing some contaminants undergoes to a venation-like morphology with uniformly distributed porous of SC-A500. The venation structure is a continuous phase non-separated by porous which were formed by the complete decomposition of PVP at annealing temperature. Moreover, there is no any agglomeration, particle formation nor fracturing as seen from the images. The surface and edges of the veins are very smooth. It seems like a composite structure with porous as reinforcement inside  $V_2O_5$

matrice. However, there are some cracks on veins having just a few nanometers in length when look closely. It can be understood that the smoothness of the edges of the veins and fracturing-free morphology confirm XRD results that the crystallinity of the film is low.

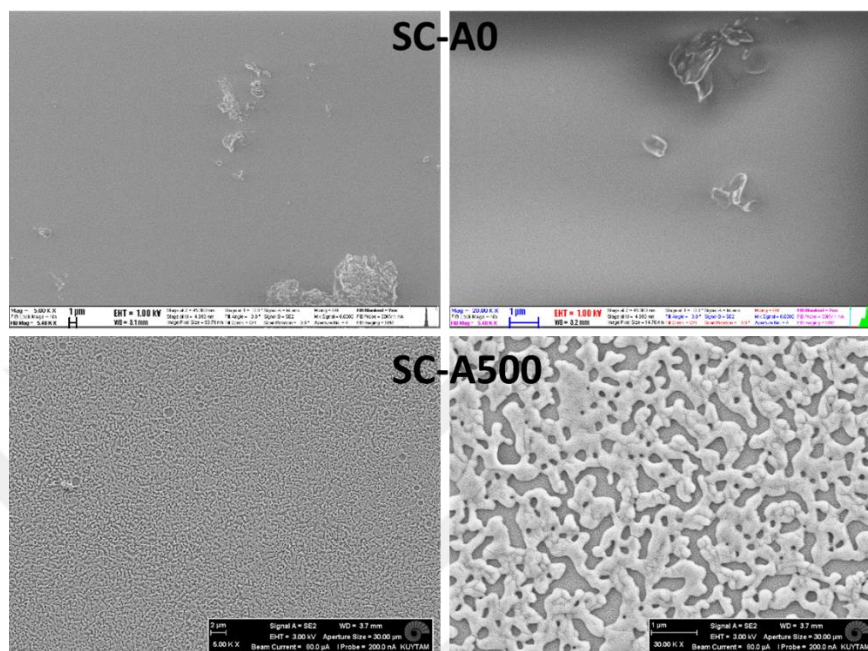


**Figure 4.7 :** SEM images of SC-A500.

SEM micrographs of SC-B0 and SC-C0 with 5K and 20K magnifications are given in Figure 4.5. Both SC-B0 and SC-C0 look like having smooth and uniform surfaces as seen at 5K magnification. However, it is clearly seen from the 20K magnified SEM images that the surfaces are actually not smooth. The spindle-like surface of the samples is expected to be associated with the bundles of rods. The SC-C0 has smoother surface than SC-B0 as seen from 20K magnification micrographs. It can be deduced that bundled rods of SC-C0 sample are smaller. By the way, it should be noted that the structures seen on 5K magnituded SEM images of the samples are impurities which helped us to focus the surfaces during SEM analyze.

SEM images of annealed samples SC-B500 and SC-C500 with 5K and 20K magnification are shown in Figure 4.6. Both SC-B500 and SC-C500 samples consist of planar-grown nanorods. The width and length of the nanorods of SC-B500 are measured as approximately 250 to 500 nm and 1 to 3.1  $\mu\text{m}$ , respectively. By aging, the nanorods of SC-C500 seem shrunk in width, about 210 to 340 nm, while their length remained the same. Besides, the nanorods of SC-C500 sample have smoother surfaces.

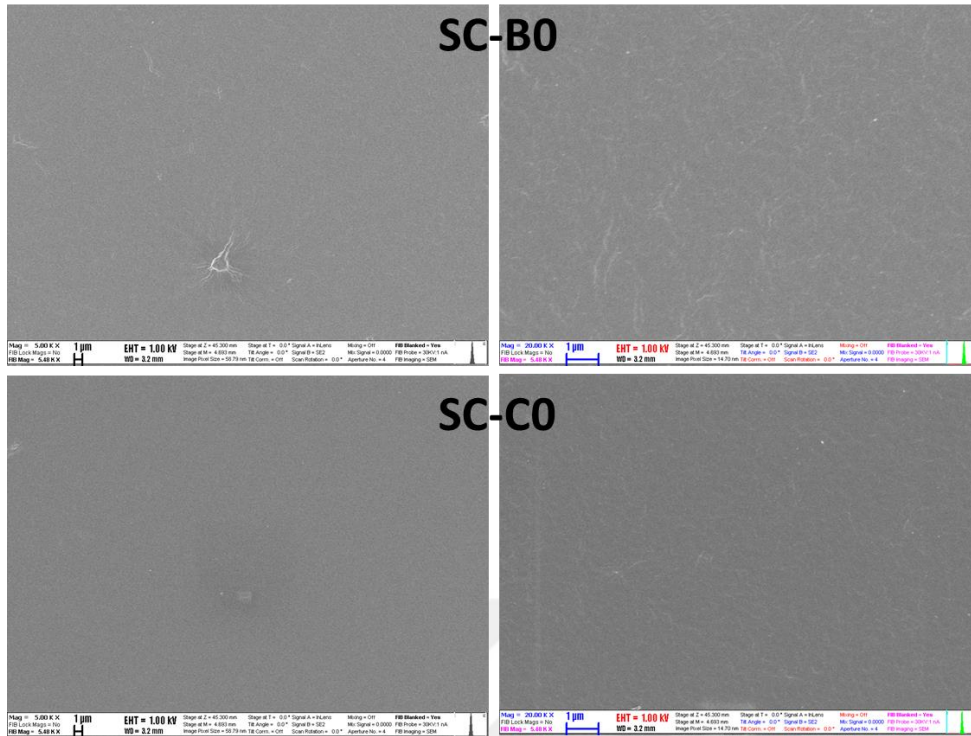


**Figure 4.8 :** 5K (left) and 20K (right) magnified SEM micrographs of SC-B0 (top) and SC-C0 (bottom).

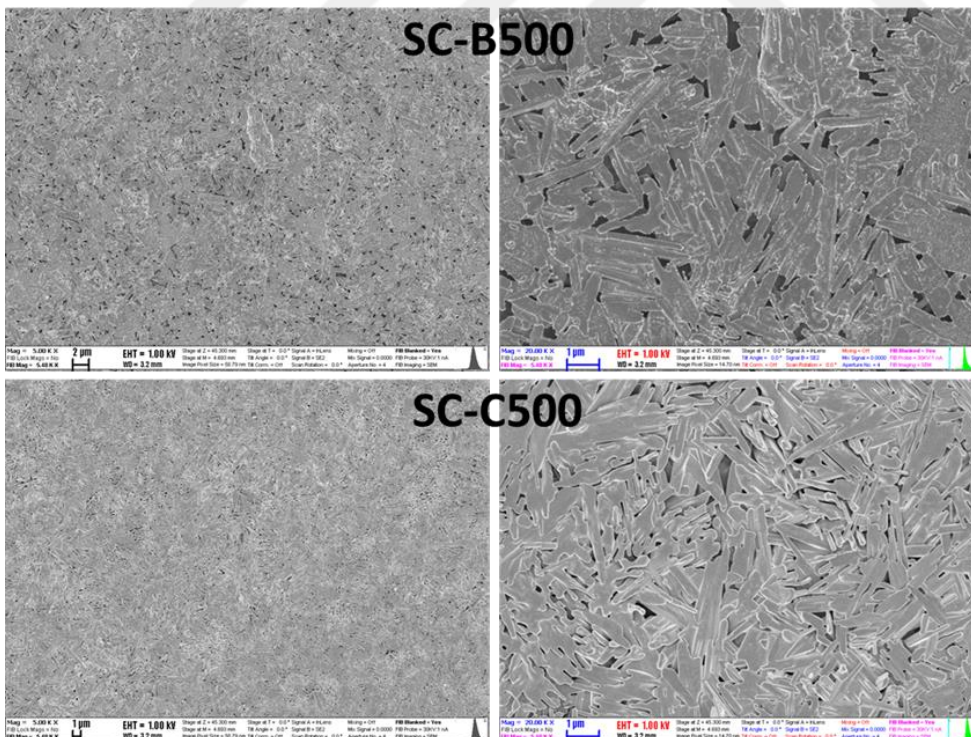


**Figure 4.9 :** 5K (left) and 20K (right) magnified SEM images of SC-B500 (top) and SC-C500 (bottom).

It is clearly seen from Figure 4.5 and 4.6 that aging has influence on not only the solution but also the film obtained from the solutions. Both rods of the solutions and nanorods produced after annealing decrease in width by aging.

## 4.2 Optical Properties

The optical properties of vanadium oxide samples deposited on microscope slides were analyzed at room temperature in air atmosphere by a UV-Vis spectrophotometer. Both transmittance and absorbance values of the samples recorded between 300 nm to 900 nm of wavelength by the spectrophotometer.

The UV-visible transmittance spectra of the vanadium oxide samples deposited onto microscope slides are shown in Figure 4.7. There are sharp decreases in transmission of some samples. The transmissivity of SC-A start decreasing below 490 nm, while transmittances of SC-B0, SC-C0 and SC-C500 decreases below approximately 600 nm. These decreases are related to the fundamental absorption edges. As seen from the figure, SC-A0 has the highest transmittance percentage, which is 94% in the visible region. However, its annealed form, SC-A500, has very low transmittance, is nearly opaque. The relationship between transmittance of NF-A0 and NF-A500 is unlike their thin film-formed counterparts SC-A0 and SC-A500. The transmissivity increases from 46% to approximately 80% in the visible region as nanofibers annealed at 500°C. On the other hand, only NF-A500 is transparent in the whole region, 300-900 nm. The difference between SC-A0 and NF-A0 in the visible region is expected because of the reflection of the electromagnetic radiation through the surface of the nanofibers having diameter bigger than 100 nm. However, since nanofibers shrink in diameter as annealed due to the loss of PVP, the reflection of the light decreases and thus the annealed nanofiber sample NF-A500 has higher transmissivity. SC-B0 has about 45% transmissivity, while with annealing, SC-B500 becomes almost opaque. On the other hand, its nano-structured counterpart SC-C500 has better transmittance about 65% in the visible region, and it decreases just to 43% with annealing as seen from the plot of SC-C500.

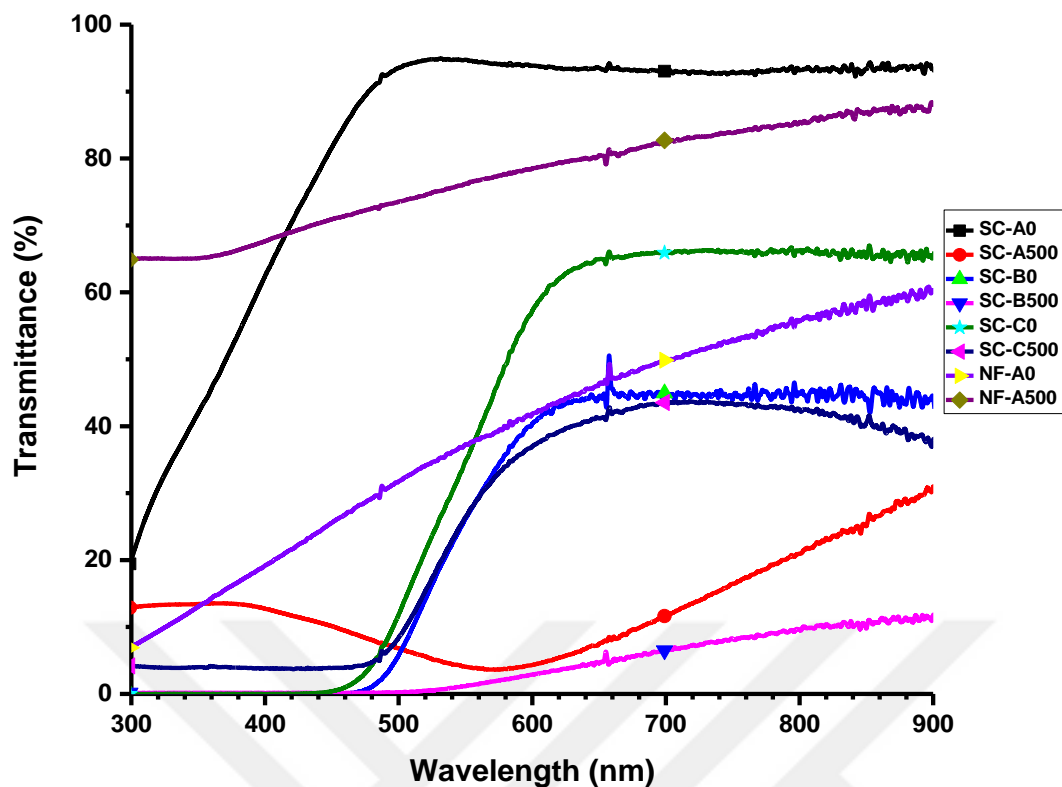


**Figure 4.10 :** Transmittance spectra of all samples coated on microscope slides within the range of 300 - 900 nm of wavelength.

Temperature dependent transmission spectra analysis of annealed vanadium-oxide films was realized at three temperatures in order to investigate the thermochromic behavior as shown in Figure 4.8-9.

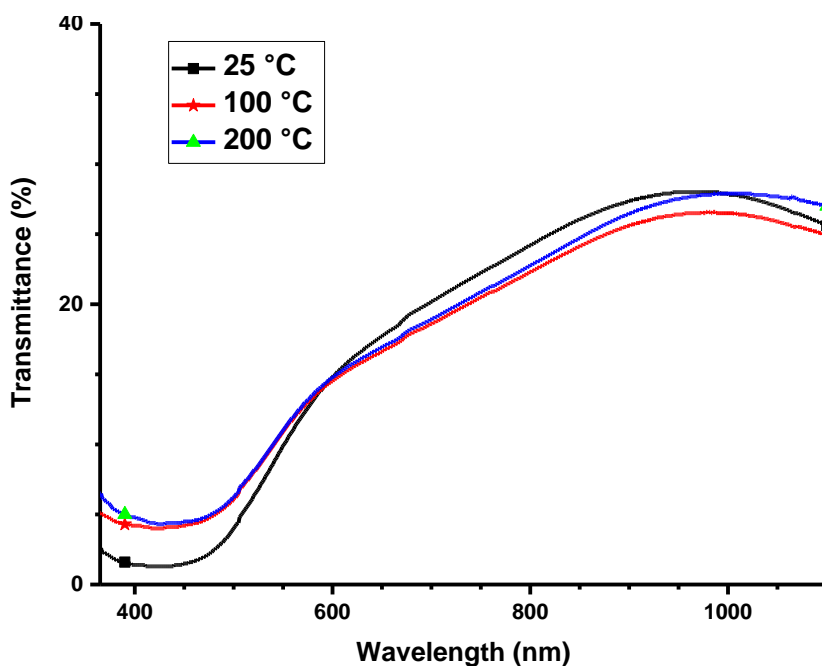


**Figure 4.11 :** Temperature dependent transmittance spectra of SC-B500

SC-A500 was in agreement with the literature that its optical properties was temperature independent up to 200°C within the region 350 to 1100 nm of wavelength. The absorption edge values of both SC-B500 and SC-C500 slightly shifted towards red wavelengths with increasing temperature from 25°C to 200°C as a sign of the thermochromic behavior. These shifts in absorption edge values lead to a gradual change in color of the films.

Measurements were also realized during cooling at 100°C and 25°C in order to investigate the reversibility of thermochromic behavior of SC-B500 and SC-C500. UV-visible spectra of both SC-B500 and SC-C500 were found exactly same with the spectra obtained while heating.

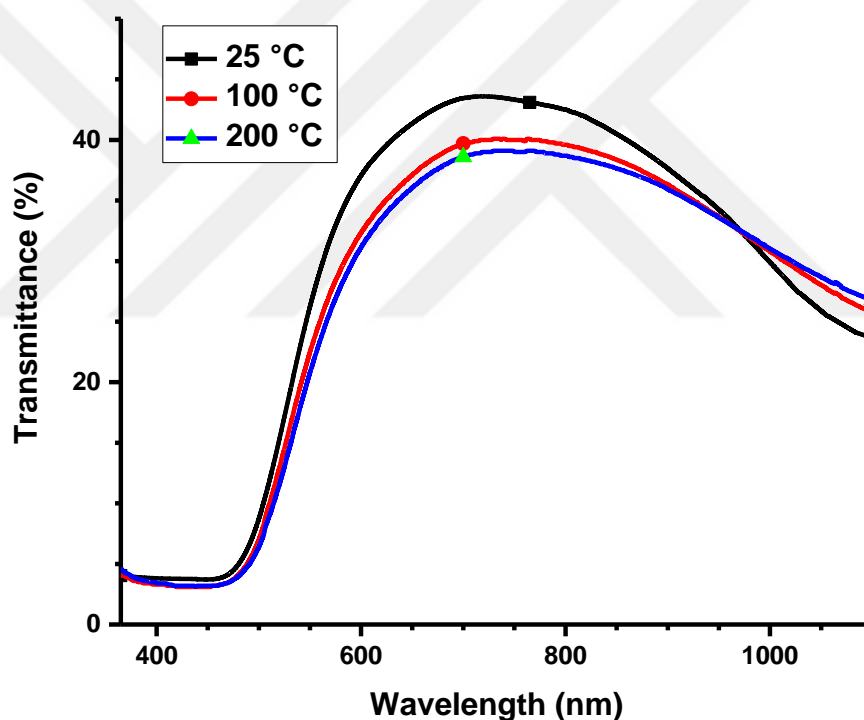


**Figure 4.12 :** Temperature dependent transmittance spectra of SC-C500

### 4.3 Electrochemical Properties

#### 4.3.1 Cyclic voltammetry

Cyclic voltammetry (CV) measurements were carried out to investigate the electrochemical behaviour of prepared samples. The CV were performed in the conventional three-electrode cell where vanadium-oxide/ITO-glass electrodes were

used as working electrode in an electrolyte of 1M LiClO<sub>4</sub> in PC at room temperature. The electrodes were cycled galvanostatically by a potentiostat in a potential range of -1V to +1V (vs. Li/Li<sup>+</sup>) at varying scan rates between 2 to 50 mV/s, starting from the slowest one 2 mV/s. Electrodes were cycled several times previous to CV measurement to achieve the steady-state voltammogram in each case.

The cyclic voltammograms, which are the plot of current versus applied voltage, of vanadium oxide electrodes at scan rates in the following order 2, 5, 10, 20 and 50 mV/s are given in Figure 4.10-13. As seen from the figures, the shape of the all obtained curves are typical diffusion-controlled CVs of highly reversible lithium intercalation/deintercalation processes.

NF-A500 and SCA-500 exhibit two well-defined peaks, two cathodic peaks appearing on cathodic scanning (discharge) and two anodic peaks appearing on anodic scan (charge) in the CV graphs. These peaks are ascribed to the redox reactions of V<sup>5+</sup>/V<sup>4+</sup> by the lithium intercalation/deintercalation. The cathodic peaks are attributed to the reduction of V<sup>5+</sup> to V<sup>4+</sup> by the insertion of Li<sup>+</sup> ions into the crystal structure of vanadium resulting of the formation of different crystalline phases of Li<sub>x</sub>V<sub>2</sub>O<sub>5</sub>. On the other hand, anodic peaks are corresponded to oxidation of V<sup>4+</sup> to V<sup>5+</sup> and deintercalation of Li<sup>+</sup> ions from the crystal structure of the electrode during charging. Having two peak is attributed to a typical two-step electrochromism; yellow to green and then green to blue. We have observed these color changes during CV measurements thanks to the electrodes made up of transparent ITO glasses. Only an amount of the V<sup>5+</sup> ions reduce to V<sup>4+</sup> in the first reduction peak, leaving a mixture of V<sup>4+</sup> and V<sup>5+</sup>, and remaining V<sup>5+</sup> ions reduces to V<sup>4+</sup> in the second reduction peak. It is similar for the two oxidation peaks, an amount of V<sup>4+</sup> oxidize to V<sup>5+</sup> in the first peak resulting a mixture of V<sup>4+</sup> and V<sup>5+</sup>, then the remained V<sup>4+</sup> ions oxidize at the second oxidation peak. The separation of both cathodic and anodic peaks, and the intensity of peaks increase with increasing scan rate. Since surface charge storage occurs faster than diffusion-based charge storage, the distinct Li<sup>+</sup> insertion and removal peaks that are observed at slow scan rates are not as well defined at higher scanning rates.

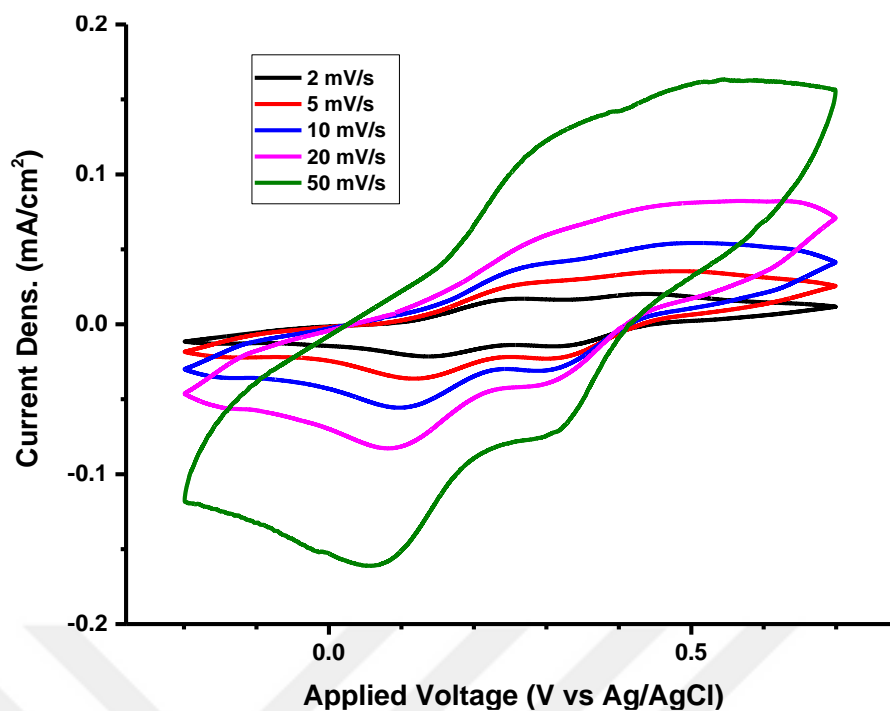


**Figure 4.13 :** Cyclic voltammogram of NF-A500.

The anodic peaks of the nanofiber NF-A500 occurs at around 0.25 and 0.44 V/Li, while cathodic peaks are present at 0.14 and 0.32 V/Li for 2 mV/s of the scan rate. These redox peaks shift and the separation between anodic and cathodic peaks grows as the scan rate increases.

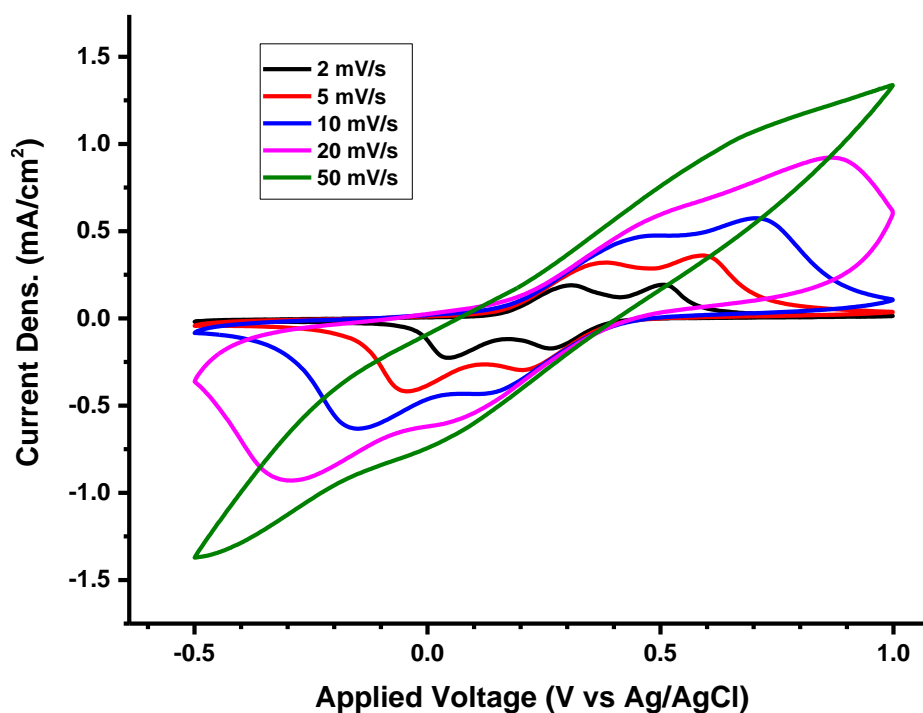


**Figure 4.14 :** Cyclic voltammogram of SC-A500.

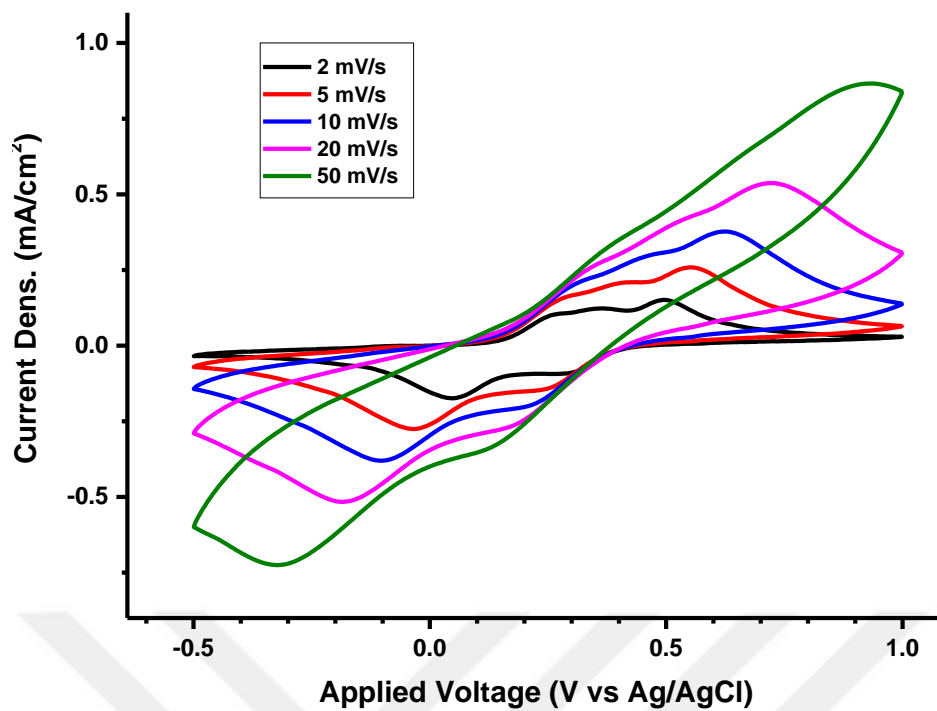


Figure 4.15 : Cyclic voltammogram of SC-B500

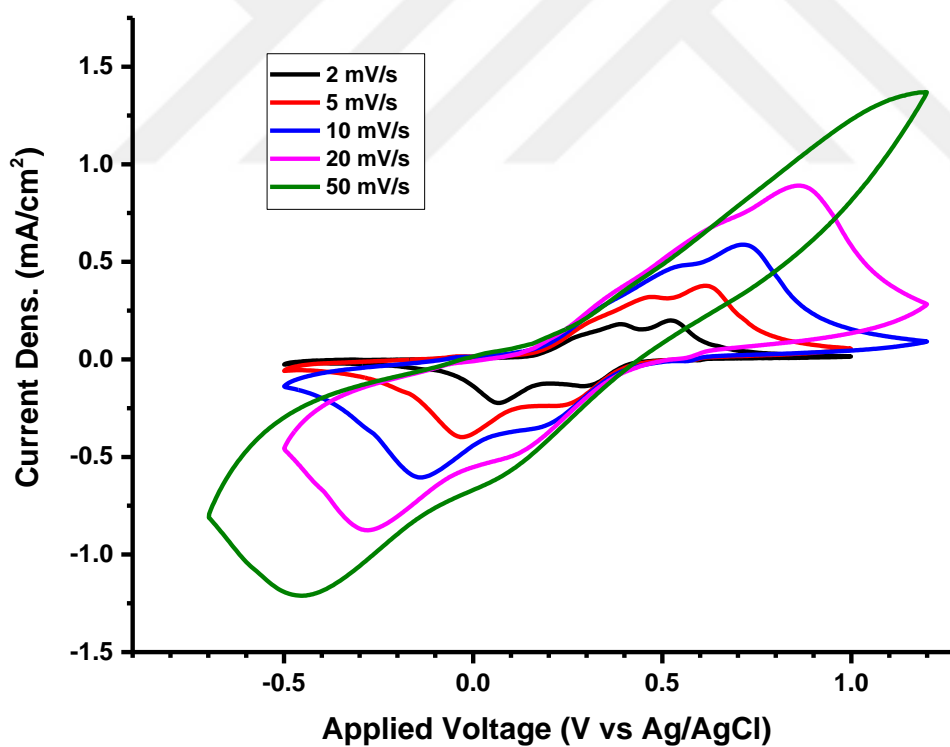


Figure 4.16 : Cyclic voltammogram of SC-C500

In order to compare electrochemical activity of the annealed samples, CVs at 10 mV/s of scan rates are given in Figure 4.14. The defined both cathodic and anodic peaks are marked as  $P_{c1}$ ,  $P_{c2}$ ,  $P_{a1}$  and  $P_{a2}$ , respectively. The potential and current densities of

corresponding cathodic and anodic peak positions are designated as Epc1, Epc2, Ipc1, Ipc2, and Epa1, Epa2, Ipa1, Ipa2, respectively. The anodic and cathodic peak potentials, corresponding current densities, differences in cathodic and corresponding anodic peak densities ( $I_{pc2} - I_{pa1}$ ) and ( $I_{pa2} - I_{pc1}$ ), and the intercalation/deintercalation capacities of NF-A500, SC-A500, SC-B500 and SC-C500 measured from the CV at a scan rate of 10 mV/s are summarized in Table 4.1.

**Table 4.1** : Peak potential and current density, intercalation/deintercalation capacity as deduced from the CV at a scan rate of 10 mV/s, together with differences in current densities of cathode and corresponding anode peaks.

	NF-A500	SC-A500	SC-B500	SC-C500
Epa1 (V vs SCE) / Ipa1 (mA/cm <sup>2</sup> )	0.3/0.03	0.13/0.43	0.22/0.20	0.17/0.35
Epa2 (V vs SCE) / Ipa2 (mA/cm <sup>2</sup> )	0.1/0.05	0.15/0.63	0.1/0.38	0.13/0.60
Epc1 (V vs SCE) / Ipc1 (mA/cm <sup>2</sup> )	0.01/5x10 <sup>-4</sup>	0.47/0.47	0.31/0.21	0.54/0.47
Epc2 (V vs SCE) / Ipc2 (mA/cm <sup>2</sup> )	0.27/0.04	0.71/0.58	0.62/0.38	0.71/0.59
Ipc2 - Ipa1 (mA/cm <sup>2</sup> )	0.01	0.15	0.18	0.24
Ipa2 - Ipc1 (mA/cm <sup>2</sup> )	0.0495	0.16	0.17	0.13
Intercalation/deintercalation capacity (mC/cm <sup>2</sup> )	0.41	0.318	0.33	0.435

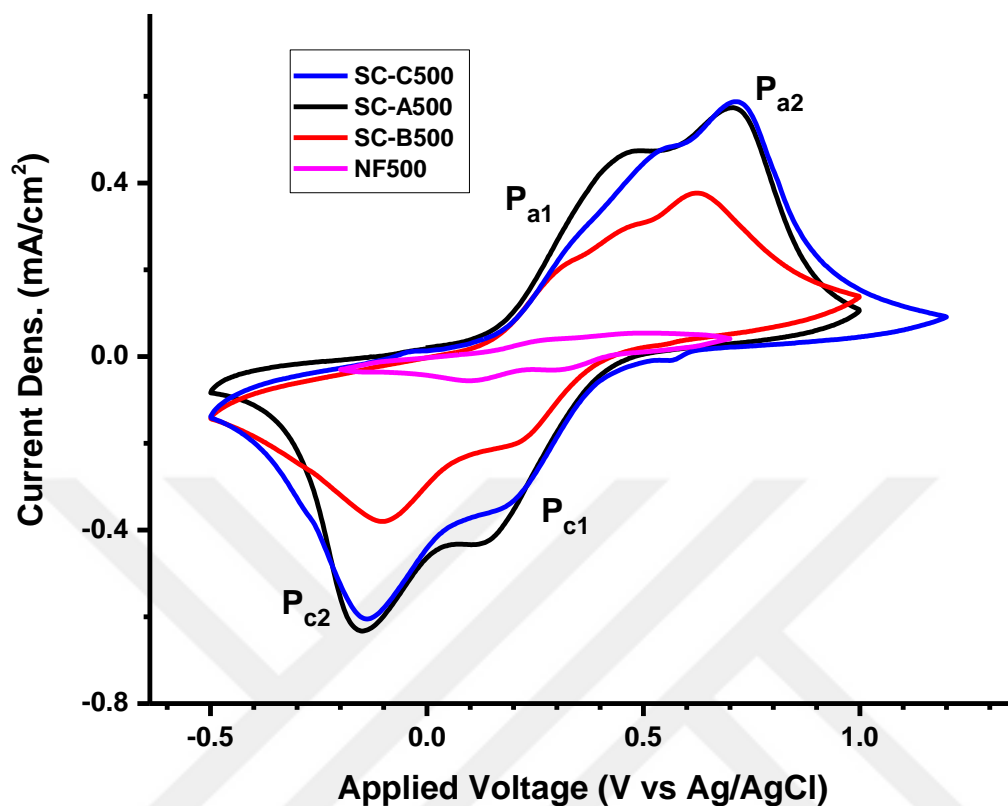


**Figure 4.17** : Cyclic voltammogram of annealed samples at a scan rate of 10 mV/s

### 4.3.2 Electrochemical impedance spectroscopy analysis

Electrochemical and interfacial properties of vanadium oxide samples deposited by different routes were examined by electrochemical impedance spectroscopy (EIS). The EIS data give information about both the nature of the electrochemical process occurring at the electrode/electrolyte interface and electronic and ionic conductivity of the electrodes. While performing EIS measurements, the whole samples exhibited electroactivity and stability without any deformation, except SC-A0 and NF-A0. Since the samples contained PVP, they were dissolved in the electrolyte and disappeared.

Nyquist plots of annealed samples, which were deposited onto ITO glass, were plotted on the complex plane as seen in Figure 4.15, while Bode Phase plots are given in Figure 4.16.

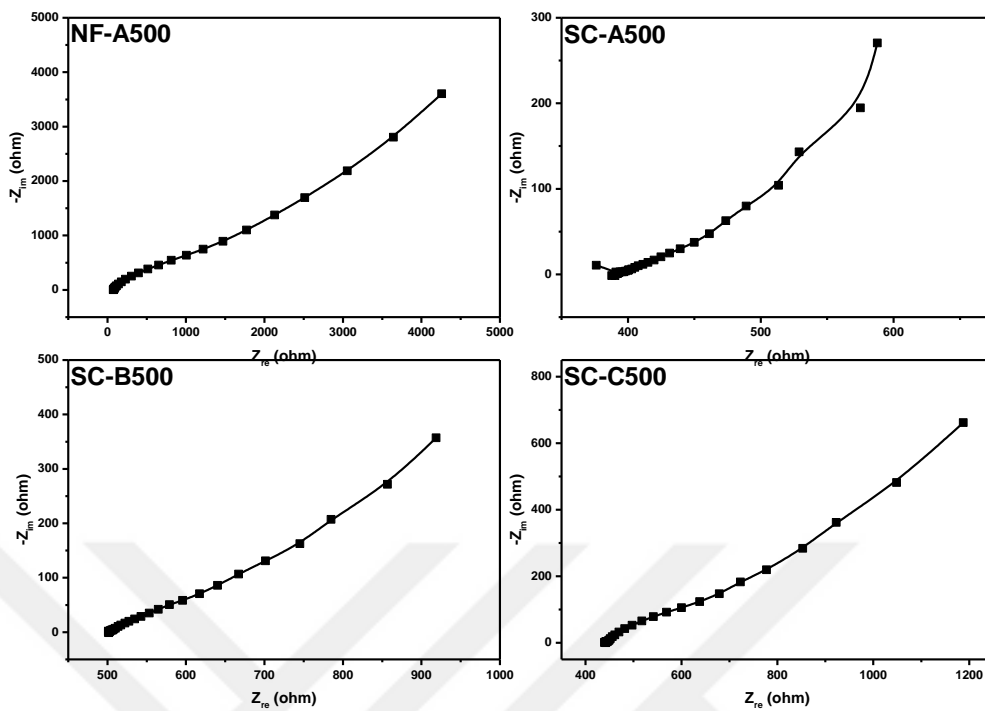


**Figure 4.18** : Nyquist plots of the annealed samples. Left top: NF-A500, right top: SC-A500, left bottom: SC-B500, right bottom: SC-C500

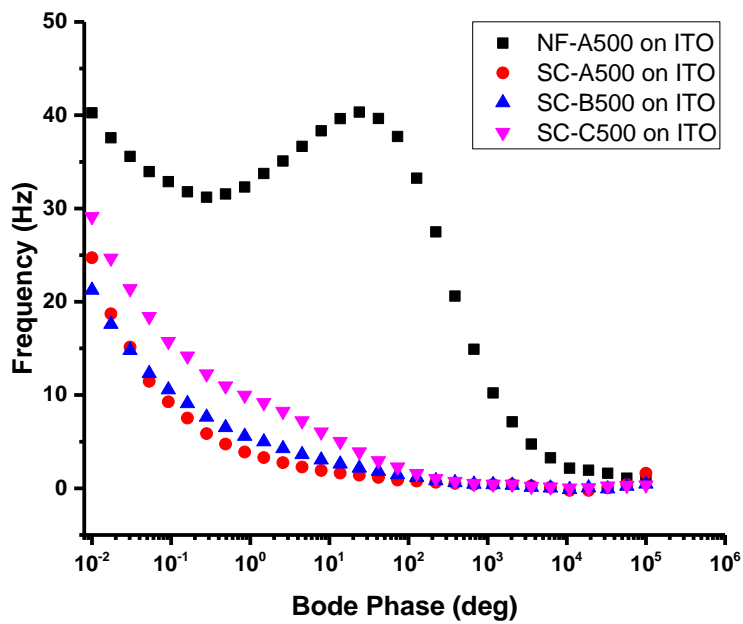


**Figure 4.19** : Bode Phase plots of annealed samples.

According to Figure 4.15, all samples exhibit sloping lines in Nyquist plots. The thin film  $V_2O_5$  electrode SC-A500 exhibits a phase angle with 21.2 degree, while the  $V_2O_5$  nanofiber electrode NF-A500 has the biggest phase angle with 40.25 degree. On the other hand, the nanostructured thin film  $V_6O_{13}$  sample SC-C500 with 29.1 degree of phase angle has better conductivity than thin film  $V_6O_{13}$  sample SC-B500 which exhibits 21.2 degrees phase angle. These informations indicates that samples with nanostructured textures have improved electrical properties compared to their thin film counterparts. Phase angles of spin coated samples SC-A500, SCB-500 and SC-C500 decrease with increasing in frequency. However, the maximum phase angle value of NF-A500 electrode changed at higher-frequency range of the Bode phase plot. This change in phase is the result of an additional capacitive element arising from deposited nanofiber layer on the ITO substrate surface and electronic behavior of the deposited layer. The highest phase angle of NF-500 in the medium-frequency region can be associated with the porous structure of the nanofibers. This reaction in medium-frequency is confirmed by the ionic and electronic conduction through porous  $V_2O_5$  nanofibers.

The equivalent circuit of the EIS data of the samples was modelled by calculated data and measured data that were fitted well with the chosen circuit seen in Figure 4.20 and by using ZSimpWin software to compute kinetics of the systems (Figure 4.17). The equivalent circuit giving information about the physical properties of the electrodes and fitting well with the measured EIS data with low Chi-squared errors and a logical number of circuit elements were chosen. The Chi-squared errors were within the range of  $10^{-4}$  magnitude, which is widely accepted as “low” and represents precise measurement.

The measured samples can be thought as layered electrodes consisting of a layer with vanadium oxide films or nanofibers, and a more compact layer, the substrate. The interfacial properties of a layered electrode brings with varied equivalent circuit models. Thus, the equivalent circuit model including resistors and capacitors was chosen to depict the ionic and electronic through non-porous/porous vanadium oxide layers and a high-frequency time constant for the compact layer at the interface between vanadium oxide and the substrate. Besides, it is a requirement to appoint a constant phase element (CPE) to factor in the disorders of the electrode structures. The chosen circuit model also elucidates the interfacial charge transfer of the vanadium

oxide surfaces in touch with the electrolyte, and the reactions in the pores and solid vanadium layers. The resistance of the solution and the resistance-capacitance phenomena happening at the vanadium oxide-substrate interface are prevalent at higher-frequency range.

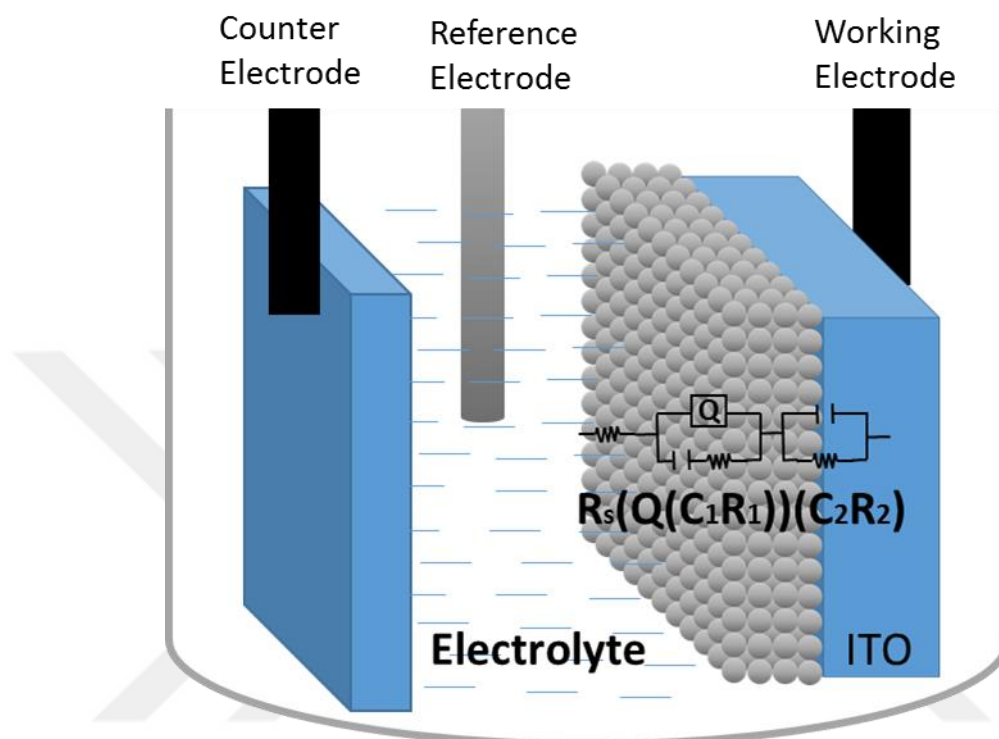


**Figure 4.20** : Schematic representation of electrochemical experimental setup, and equivalent circuit modelling of vanadium-oxide/SnO<sub>2</sub>:In electrodes (inside).

The EIS data of the samples were modelled by the equivalent circuit of  $R_s(Q(CR))(CR)$  as given in Figure 4.17. The resistors and capacitors describes various complex interfacial reactions between vanadium oxide layers, substrates and the electrolyte. The first element of the circuit,  $R_s$ , is the solution resistance of the electrolyte. It is described as the sum total of resistances that are because of the existence of the electrolyte on the electrode surface.  $R_s$  value of NF-A500 and SC-A500 samples deposited onto ITO glass were found as 77.3 and 388.8  $\Omega$ , respectively. The  $R_s$  is about the behaviour of the electrolyte, which fills pores of vanadium oxide layers. The thin film sample SC-A500 has higher solution resistance because of including more porous than nanofiber sample. On the other hand, the  $R_s$  values of V<sub>6</sub>O<sub>13</sub> samples SC-B500 and SC-C500 were found as 499.5 and 439.3, respectively.

Q accounts for the constant phase element (CPE) which is taken in to account due to the inhomogeneity in conductance. CPE is described by the formula of

$$Z_{CPE} = T_{CPE}(j\omega)^{-n} \quad (4.2)$$

Where  $T_{CPE}$  and  $n$  are frequency-independent constants, and  $\omega$  is the angular frequency. The exponentiation of  $n$ , resulting from the slope of the  $\log(Z)$  vs.  $\log(f)$  plot, is a manifestation of the electrode nature, and a correcting variable for the inhomogeneity of the electrode and roughness of its surface. The  $n$  value ranges from 0 to 1. It means the CPE element is an ideal capacitor if  $n=1$ , while  $n=0$  and  $n=0.5$  are related to resistance and Warburg behaviours, respectively.

The fitting parameters of the modelled equivalent circuit for EIS data were given in Table 4.1. The  $n$  values of  $V_2O_5$  samples NF-A500 and SC-A500 were found as 0.41 and 0.32, while  $V_6O_{13}$  samples SC-B500 and SC-C500 have 0.33 and 0.435, respectively. It indicates that nanostructured samples NF-A500 and SC-C500 has lower capacitive behaviours compared to their film structures. The nanostructured samples have more surface area, thus the diffusions of the ions are easier.

The first capacitor element of the equivalent circuit,  $C_1$ , is related to the double layer capacitance,  $C_{dl}$ , of the vanadium oxide layer between electrolyte and the surface of the substrate.  $C_{dl}$  is based on the alignment of solute counter ions along the electrode surface. The electron transfer through the electrode happens by overcoming solution resistance, activation barrier and charge transfer resistance. As soon as the electron transfer begins through the electrode, the electrode kinetics is defined by Warburg impedance (W) because of the mass transport. Comparing  $V_2O_5$  samples,  $C_1$  of NF-A500 was slightly higher than of SC-A500, which were found as  $8.434 \times 10^{-6}$  and  $1.026 \times 10^{-6}$  F/cm<sup>2</sup>, respectively. On the other hand, there was a huge difference in  $C_1$  values of  $V_6O_{13}$  samples SC-B500 and SC-C500, which were calculated as  $2.186 \times 10^{-5}$  and  $2.578 \times 10^{-3}$ .

$C_2$  symbolizes the capacitance of the interface between the vanadium oxide surface and the coated surface of the substrate. The variation of  $C_2$  values can be interpreted by the varying structures formed at substrate surfaces, such as  $V_2O_5$  or  $V_6O_{13}$ , and nanofiber, nanorod or film.

**Table 4.2 :** Fitting values of the modelled equivalent circuit elements by the simulation of the Nyquist plots of annealed samples.

Circuit Elements	NF-A500	SC-A500	SC-B500	SC-C500
$R_s (\Omega) (x10^{-5})$	77.29	388.8	499.5	439.3
$Q (x10^{-5})$	38.55	1006	511.2	297.5
$C_1 (\mu F/cm^2)$	8.4	1	21.8	2578
$R_1 (\Omega)$	7304	$3.85 \times 10^{-22}$	16.29	2894
$C_2 (F/cm^2) (x10^{-5})$	599.2	9614	13520	102.4
$R_2 (\Omega)$	$1.75 \times 10^{-4}$	$9.2 \times 10^{-20}$	$1.14 \times 10^{-12}$	39.77
$n (0 < n < 1)$	0.41	0.318	0.33	0.435
Chi-sq. ( $x10^{-4}$ )	9.39	1.76	0.22	0.39

The R elements of the equivalent circuit represent the charge transfer resistances ( $R_{ct}$ ) of interfaces between vanadium oxide surface and electrolyte, and vanadium oxide surface and the coated surface of the substrate.  $R_1$  represents the charge transfer resistance of the vanadium oxide - electrolyte interface.  $R_1$  values of the samples NF-A500, SC-A500, SC-B500 and SC-C500 were found as 7304,  $3.85 \times 10^{-22}$ , 16.29 and 2894 respectively. The  $R_2$  values, representing the charge transfer resistance of the vanadium oxide - substrate interface, were found as  $1.75 \times 10^{-4}$ ,  $9.2 \times 10^{-20}$ ,  $1.14 \times 10^{-12}$

and 39.77 for the samples NF-A500, SC-A500, SC-B500 and SC-C500, respectively. The conductivity of the vanadium oxide layer depends on the geometry of the contact zone between the substrate or roughness of its surface in touch with electrolyte, and also its structure such as nanorod or nanofiber etc.



## 5. CONCLUSION

In summary, nanofibers (NF-A0, NF-A500), porous structured thin film (SC-A500), well grown grassland structured nanorods and planar-grown nanorods in thin film structure (SC-B500 and SC-C500) of vanadium oxides successfully produced by facile and versatile wet chemical method from varied solutions in this thesis. Two liquid species were used to achieve producing vanadium oxides in various forms. The first liquid (Sol-A) was a solution of  $V_2O_5$  powder and PVP inside  $H_2O_2$  and water. From this solution, nanofibers, grassland-like structured nanorods and porous thin film were obtained by electrospinning, electrospraying and spin-coating techniques, respectively. In order to get the second liquid (Sol-B), which was a gel,  $V_2O_5$  powder was used instead of toxic and expensive organometallic species. PVP-free  $V_2O_5 - H_2O_2$  solution was heated to implement the polycondensation by the following of the hydrolysis reaction of the solution with air. Thin film containing planar-grown nanorods was prepared from this gel by spin coating technique. The gel was also aged (Sol-C) to see aging effect on the film structure and its properties.

According to XRD results, non-heat treated samples have amorphous structure, but SC-C, the film prepared from the aged gel. The crystalline structure has obtained without a heat treatment simply by aging the solution. Heat-treated samples deposited onto corning glasses doped with sodium atoms coming from the substrate and crystalline  $Na_{0.33}V_2O_5$  bronze species were obtained.

SEM analysis shown that the nanofibers with smooth and uniform surfaces, high aspect ratio and uniform distributed in diameter were obtained concentratedly. Bead formation also observed due to high applied voltage and the low viscosity of the solution, arising from the low PVP concentration. Nanofibers have found to be 15 – 240 nm in diameter, while average diameter was  $59.1 \pm 40$  nm.

TEM investigation indicates that non-heat treated SC-A sample has such a small crystalline phases that was not able to be detected by XRD. These crystalline phases was found to be tetragonal  $VO_2$  ( $a = 0.2851$  nm,  $b = 0.4552$  nm,  $c = 0.4552$  nm,  $\alpha =$

90 °,  $\beta = 90$  °,  $\gamma = 90$  °). Three of heat-treated samples have very similar structure, which is found by SAED patterns as monoclinic  $V_6O_{13}$  ( $a = 1.1911$  nm,  $b = 0.3674$  nm,  $c = 1.013$  nm,  $\alpha = 90$  °,  $\beta = 100.9$  °,  $\gamma = 90$  °).

The transmittance value of non-heated SC-A film with 94% was found as highest among all samples, while it turned to opaque with annealing. This huge difference is expected to be the result of the reflection of the electromagnetic radiation at vein edges. Unlike SC-A samples, transmittance of nanofibers increased with annealing due to the shrinkage of nanofibers in diameter, which decreased the reflection. The thin film prepared from aged gel (Sol-C), SC-C0 and SC-C500, had better transmittance than SC-B0 and SC-B500 prepared from non-aged gel, respectively.

SC-B500 and SC-C500 found to have reversible thermochromic properties by temperature dependent UV-Vis. analysis. Their adsorption edge values were shifted towards red wavelength and transmittance decreased gradually with increasing temperature.

All four of annealed samples exhibited typical diffusion-controlled CVs of highly reversible intercalation/deintercalation processes with well-defined two peak pairs. The separation of anodic and cathodic peaks, and the intensities of the peaks increased with increasing scan rate, which is associated with higher surface charge storage than diffusion-based charge storage. Having two peak pairs, which is expected to be a result of the layered structure of vanadium oxide, is attributed to a typical two-step electrochromism; yellow to green, and green to blue as seen from Figure 5.1. SC-C500 was found to have the highest intercalation/deintercalation capacity.

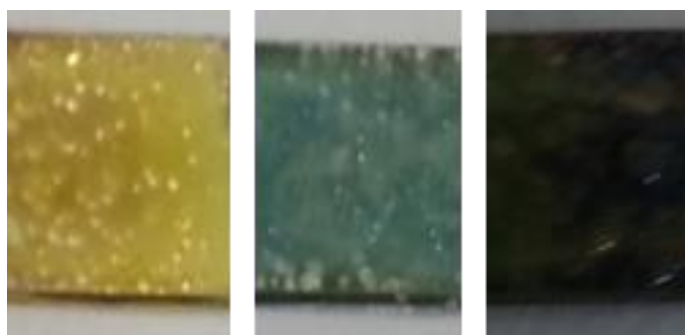


**Figure 5.1** : Electrochromic photograph of SC-B500 film taken at 700, 300, and -200 mV applied potentials from left to right, respectively.

According to Bode phase plots of annealed samples obtained from EIS analysis, NF-A500 had the best conductivity. To see the aging effect, SC-C500 prepared from aged gel had better conductivity than SC-B500. While phase angle values of spin coated samples decreased with increasing frequency, the maximum phase angle value of nanofibers found at higher frequency of Bode phase plot, which is the result of an additional capacitive element arising from nanofiber layer.

Experimental EIS spectra were fitted well to the calculated data which was obtained from equivalent circuit modelling with  $(R_s(Q(C_1R_1)(C_2R_2)))$ , with  $10^{-4}$  magnitude of Chi-squared errors.  $R_s$ , the solution resistance of the electrolyte, is described as the sum total of resistances that are because of the existence of the electrolyte on the electrode surface. It is about the behavior of the electrolyte, which fills pores of vanadium oxide layers.  $Q$  accounts for the constant phase element (CPE) which is taken in to account due to the inhomogeneity in conductance. The  $n$  value, ranging from 0 to 1, means the CPE element is an ideal capacitor if  $n=1$ , while  $n=0$  and  $n=0.5$  are related to resistance and Warburg behaviors.  $C_1$ , is related to the double layer capacitance,  $C_{dl}$ , of the vanadium oxide layer between electrolyte and the surface of the substrate.  $C_{dl}$  is based on the alignment of solute counter ions along the electrode surface.  $C_2$  symbolizes the capacitance of the interface between the vanadium oxide surface and the coated surface of the substrate.  $R_1$  and  $R_2$  represent the charge transfer resistance ( $R_{ct}$ ) of the vanadium oxide - electrolyte interface and of the vanadium oxide - substrate interface, respectively.



## REFERENCES

- [1] **Ettu, O.** (2014). The role/importance of engineering materials utilization in present day world, *International Journal of Engineering Development and Research*, 3 (1), 2321-9939.
- [2] **Url-1** <<http://www.engineeringchallenges.org>>, data retrieved 13.04.2017.
- [3] **Thavasi, V., Singh G. & Ramakrishna, S.** (2008). Electrospun nanofibers in energy and environmental applications, *Energy & Environmental Science*, 1 (2), 205.
- [4] **Modafferia, V., Panzeraa, G., Donatoa, A., Antonuccia, P.L., Cannillab, C., Donatoc, N., Spadarod, D., & Nerid, G.** (2012). Highly sensitive ammonia resistive sensor based on electrospun V2O5 fibers, *Sensors and Actuators B: Chemical*, 163 (1), 61-68.
- [5] **Lan, S., Cheng, C., Huang, C., & Chen, J.** (2015). Synthesis of sub-10 nm VO2 nanoparticles films with plasma-treated glass slides by aqueous sol-gel method, *Applied Surface Science*, 357 (B1), 2069-2076.
- [6] **Sethupathy, M., Ravichandran, S., & Manisankar, P.** (2014). Preparation of PVdF-PAN-V2O5 hybrid composite membrane by electrospinning and fabrication of dye-sensitized solar cells, *International Journal of Electrochemical Science*, 9, 3166 – 3180.
- [7] **Wang, Y., & Chen, C.** (2013). Facile growth of thermochromic VO2 nanostructures with greatly varied phases and morphologies, *Inorganic Chemistry*, 52 (5), 2550–2555.
- [8] **Najdoski, M., Koleva, V., & Samet, A.** (2014). Effect of deposition conditions on the electrochromic properties of nanostructured thin films of ammonium intercalated vanadium pentoxide xerogel, *The Journal of Physical Chemistry C*, 118 (18), 9636–9646.
- [9] **Chudnovskiy, F., Luryi, S., & Spivak, B.** (2002). Switching device based on first-order metal-insulator transition induced by external electric field. In S. Luryi, J. Xu, A. Zaslavsky (Eds.), *Future Trends in Microelectronics: the Nano Millennium* (pp. 148-155).
- [10] **Wang, H., Gao, X., Feng, J., & Xiong, S.** (2015). Nanostructured V2O5 arrays on metal substrate as binder free cathode materials for sodium-ion batteries, *Electrochimica Acta* 182, 769-774.
- [11] **Surnev, S., Ramsey, M.G., & Netzer, F.P.** (2003). Vanadium oxide surface studies, *Progress in Surface Science*, 73 (4–8), 117-165.
- [12] **Morin, F.J.** (1958). Oxides of the 3d transition metals, *Bell Labs Technical Journal*, 37 (4), 1047–1084.
- [13] **Morin F.J.** (1959). Oxides which show a metal-to-insulator transition at the Neel temperature, *Physical Review Letters*, 3, 34.

- [14] **Adler, D. & Feinleib, J.** (1967). Semiconductor-to-metal transition in V<sub>2</sub>O<sub>3</sub>, *Physical Review*, 155, 841.
- [15] **Adler, D.** (1968). Mechanisms for metal-nonmetal transitions in transition-metal oxides and sulfides, *Reviews of Modern Physics*, 40, 714.
- [16] **Chen, J., Yu, X., Zhu, X., Zheng, C., Gao, X., & Cen, K.** (2015). Electrospinning synthesis of vanadium–TiO<sub>2</sub>–carbon composite nanofibrous membranes as effective catalysts for the complete oxidation of low-concentration acetone, *Applied Catalysis A: General*, 507, 99–108.
- [17] **Kovendhan, M., Joseph, D.P., Manimuthu, P., Sendilkumar, A., ..... Mohan, R.** (2015). Prototype electrochromic device and dye sensitized solar cell using spray deposited undoped and ‘Li’ doped V<sub>2</sub>O<sub>5</sub> thin film electrodes, *Current Applied Physics*, 15 (5), 622–631.
- [18] **Biette, L., Carn, F., Maugey, M., Achard, M., Maquet, J., Steunou, N., ..... Backov, R.** (2005). Macroscopic fibers of oriented vanadium oxide ribbons and their application as highly sensitive alcohol microsensors, *Advanced Materials*, 17 (24), 2970–2974.
- [19] **Balasubramanian, S., & Purushothaman, K.K.** (2015). Carbon coated flowery V<sub>2</sub>O<sub>5</sub> nanostructure as novel electrode material for high performance supercapacitors, *Electrochimica Acta*, 186, 285–291
- [20] **Tong, Z., Lv, H., Zhang, X., Yang, H., Tian, Y., Li, N., Zhao, J., & Li, Y.** (2015). Novel morphology changes from 3D ordered macroporous structure to V<sub>2</sub>O<sub>5</sub> nanofiber grassland and its application in electrochromism, *Scientific Reports*, 5, 16864.
- [21] **McNulty, D., Buckley, D.N., & O’Dwyer, C.** (2014). Polycrystalline vanadium oxide nanorods: growth, structure and improved electrochemical response as a li-ion battery cathode material, *Journal of The Electrochemical Society*, 161 (9), A1321–A1329.
- [22] **Yu, D., Chen, C., Xie, S., Liu, Y., Park, K., Zhou, X., Zhang, Q., Li, J. & Cao, G.** (2011). Mesoporous vanadium pentoxide nanofibers with significantly enhanced Li-ion storage properties by electrospinning, *Energy & Environmental Science*, 4, 858–861
- [23] **Greiner, A. & Wendorff, J.H.** (2007). Electrospinning: a fascinating method for the preparation of ultrathin fibers, *Angewandte Chemie*, 46 (30), 5670–5703.
- [24] **Viswanathamurthi, P., Bhattarai, N., Kim, H.Y. & Lee, D.R.** (2003). Vanadium pentoxide nanofibers by electrospinning, *Scripta Materialia* 49 (6), 577–581.
- [25] **Julien, C., Poniatowski, E., López, C., Alarcón, E. & Jarquín, J.** (1999). Growth of V<sub>2</sub>O<sub>5</sub> thin films by pulsed laser deposition and their applications in lithium microbatteries, *Materials Science and Engineering: B*, 65 (3), 170–176.
- [26] **Q. Guo, Q., Kim, D.Y., Street, S.C., & Goodman, D.W.** (1998). Ordered binary oxide films of V<sub>2</sub>O<sub>3</sub> (0001) on Al<sub>2</sub>O<sub>3</sub>, *Journal of Vacuum Science & Technology A: Vacuum, Surfaces, and Films*, 17 (4), 1887–1892.

- [27] **Zhang, D., Zhu, M., Liu, Y., Yang, K., Liang, G., Zheng, Z., Cai, X. & Fan, P.** (2016). High performance VO<sub>2</sub> thin films growth by DC magnetron sputtering at low temperature for smart energy efficient window application, *Journal of Alloys and Compounds*, 659, 198-202.
- [28] **C.E. Patil, C.E., Tarwal, N.L., Jadhav, P.R., Shinde, P.S., Deshmukh H.P., ..... Patil, P.S.** (2014). Electrochromic performance of the mixed V<sub>2</sub>O<sub>5</sub>-WO<sub>3</sub> thin films synthesized by pulsed spray pyrolysis technique, *Current Applied Physics*, 14, 389-395.
- [29] **Vernardou, D., Louloudakis, D., Katsarakis, N., Koudoumas, E., ..... Povey, I.M.** (2015). Electrochemical evaluation of vanadium pentoxide coatings grown by AACVD, *Solar Energy Materials and Solar Cells*, 143, 601-605.
- [30] **Li, D., Huang, W., Song, L. & Shi, Q.** (2015). Thermal stability of VO<sub>2</sub> thin films deposited by sol-gel method, *Journal of Sol-Gel Science and Technology*, 75 (1), 189-197.
- [31] **Livage, J.** (1999). Optical and electrical properties of vanadium oxides synthesized from alkoxides, *Coordination Chemistry Reviews*, 190-192, 391-403.
- [32] **Livage, J.** (1984). Structure and properties of vanadium pentoxide gels, *MRS Online Proceedings Library*, 32, 125.
- [33] **Ostermann, W.** (1922). *2nd. Wissenschaften in Hamburg*, 1 (17).
- [34] **Passerini, S., Chang, D., Chu, X., Ba Le, D. & Smyrl, W.** (1995). Spin-coated V<sub>2</sub>O<sub>5</sub> xerogel thin films: 1. microstructure and morphology, *Chemistry of Materials*, 7 (4), 780-785.
- [35] **J.G. Zhang, J.G., Liu, P., Turner, J.A., Tracy, C.E. & Benson, D.K.** (1998). Highly stable vanadium oxide cathodes prepared by plasma-enhanced chemical vapor deposition, *Journal of The Electrochemical Society*, 145 (6), 1889-1892.
- [36] **Xu, X.Y. & Li, X.G.** (2005). Preparation of single crystalline V<sub>6</sub>O<sub>13</sub> nanobelts, *Chinese Chemical Letters*, 16, 249-252.
- [37] **Pedro, C.** (2004). The road to chemical names and eponyms: discovery, priority, and credit, *Angewandte Chemie International Edition*. 43 (44), 5888-94.
- [38] **Sefström, N. G.** (1831). Ueber das vanadin, ein neues metall, gefunden im stangeneisen von eckersholm, einer eisenhütte, die ihr erz von taberg in småland bezieht, *Annalen der Physik und Chemie*, 97, 43-49.
- [39] **Roscoe, H.E.** (1869). Researches on vanadium: Part II, *Proceedings of the Royal Society of London*. 18 (114-122), 37-42.
- [40] **Frederick, B.** (2003). Managing technological innovation: competitive advantage from change. Retrieved from <http://books.google.com/books> (Original work published 2011).
- [41] **Url-2** <<https://en.wikipedia.org/wiki/Vanadium>>, date retrieved 17.04.2017.
- [42] **Url-3** <<https://sciencenotes.org/vanadium-facts/>>, date retrieved 19.04.2017.

- [43] **YangYang, Y., Mao, H. & Selleby, M.** (2015). Thermodynamic assessment of the V–O system, *Calphad*, *51*, 144-160.
- [44] **Wriedt, H.A.** (1989). The O-V (oxygen-vanadium) system, *Bulletin of Alloy Phase Diagrams*, *10* (3), 271–277.
- [45] **Bahlawane, N. & Lenoble, D.** (2014). Vanadium oxide compounds: structure, properties, and growth from the gas phase, *Chemical Vapor Deposition*, *20* (7-8-9), 299–311.
- [46] **Lamsal, C. & N. M. Ravindra, N.M.** (2014). Vanadium oxides for energy and security applications. In Y. Dwivedi, S.B. Rai, J.P. Singh (Eds), *Spectroscopic Techniques for Security, Forensic and Environmental Applications* (pp. 195-220).
- [47] **Pragna Kiria, P., Hyettb, G. & Binionsa, R.** (2010). Solid state thermochromic materials, *Advanced Materials Letters*, *1* (2), 86-105.
- [48] **Niklassona, G.A. & Granqvista, C.G.** (2007). Electrochromics for smart windows: thin films of tungsten oxide and nickel oxide, and devices based on these, *Journal of Materials Chemistry*, *17*, 127-156.
- [49] **Lampert, C.M.** (2004). Chromogenic smart materials, *Materialstoday*, *7* (3), 28-35.
- [50] **Wegkamp, D. & Stähler, J.** (2015). Ultrafast dynamics during the photoinduced phase transition in VO<sub>2</sub>, *Progress in Surface Science*, *90* (4), 464-502.
- [51] **Url-4** <<https://www.gelest.com/applications/sol-gel-applications/>>, date retrieved 19.04.2017.

## CURRICULUM VITAE



**Name Surname** : Musa Erol  
**Place and Date of Birth** : Kahta, 1986  
**E-Mail** : MEROL87@GMAIL.COM

### EDUCATION

- :
- **B.Sc.** : Gebze Insitute of Technology, Materials Science and Engineering, 2011

### PROJECTS

- Düzgün Gözeneklilikte Teknik Tekstiller İçin Santrifüj Egirme Tasarımı ve İmalatı, TUBITAK PROJECT, Scholarship, 15.03.2014-15.09.2015

### REFEREED PPUBLICATIONS

- ÇALISIR M.D.,EROL M.,KILIÇ A.,AVCI H. (2016). Photophysical properties of phosphorescent elastomeric composite nanofibers. Dyes and Pigments, 125, 95-99., Doi: 10.1016/j.dyepig.2015.09.036

### INTERNATIONAL CONFERENCES

- ÇALISIR M.D.,EROL M.,SIMSEK R.,DEMİR A.,SOLAK N.,KILIÇ A. (2014). PHOSPHORESCENT BLEND NANOFIBERS: CHARACTERIZATION OF PHOTOPHYSICAL PROPERTIES. The Sixth International Conference of Applied Research on Textile (Tam metin bildiri)

- SIMSEK R.,ÇALISIR M.D.,EROL M.,KILIÇ A. (2014). Phosphorescent composite nanofibers: effect of polymer type. 6th International Conference on The Future Technical Textile (Poster)
- SIMSEK R.,EROL M.,ÇALISIR M.D.,KILIÇ A. (2014). A novel method to produce hydrophobic surface: inorganic material doped stabilized-PAN nanofiber. 6th International Conference on The Future Technical Textile (Tam metin bildiri)
- PAMPAL E.S.,STOJANOVSKA E.,EROL M.,YALÇIN H.,YAVUZ N.,KILIÇ A. (2014). Improving Lithium-ion Battery Performance via Decorating Carbon Nanofibers with Silica. E-MRS 2014 Fall Meeting (Tam metin bildiri)

